A&A, 714, A14 (2026)
https://doi.org/10.1051/0004-6361/202558495
© The Authors 2026

Astronomy & Astrophysics

Chemodynamical evidence of the HR 1614 moving group as a bar resonance*

Andreas J. Koch-Hansen[1,**], Vladislav Gulaev[1], Dominik H. Plonka[2], Camilla Juul Hansen[2], Andrew McWilliam[3], Victor P. Debattista[4], and Zdenek Prudil[5]

[1] Zentrum für Astronomie der Universität Heidelberg, Astronomisches Rechen-Institut, Mönchhofstr. 12, 69120 Heidelberg, Germany
[2] Goethe University Frankfurt, Institute for Applied Physics, Max-von-Laue Straße 12, 60438 Frankfurt am Main, Germany
[3] Carnegie Observatories, 813 Santa Barbara St., Pasadena, CA 91101, USA
[4] Jeremiah Horrocks Institute, University of Central Lancashire, Preston PR1 2HE, UK
[5] European Southern Observatory, Karl-Schwarzschild-Strasse 2, 85748 Garching bei München, Germany

Received 9 December 2025 / Accepted 15 July 2026

ABSTRACT

Moving groups (MGs) are ensembles of disk stars that clump in velocity and action space. A multitude of explanations as to their origin has been attempted, from dissolved star clusters, to resonances with the Galactic bar, or other non-axisymmetric perturbations. The object of this work, the old HR 1614 group, has already been shown not to be a disrupted cluster in terms of its broad age and metallicity distribution. Thus, its stars have more likely been trapped by the Milky Way bar at corotation. Here, we present a new study that aims to chemically and dynamically characterize this group in the context of such a resonance. To this end, we used MIKE/Magellan high-resolution, high signal-to-noise spectra of six member stars of the HR 1614 MG to determine the chemical abundance ratios for 24 elements, several for the first time in those stars. The Fe-abundances of our sample range from +0.13 to 0.38 dex and the majority of abundance ratios are fully in line with those of metal-rich Milky Way disk stars, with few exceptions. In particular, the group's eponym, HR 1614, is enhanced in essentially all abundances and coincides with the higher-[X/Fe] trends of the Milky Way's thick disk. All elements (except S and Ca) show significant intrinsic abundance scatter that argues against this MG having formed in a contained environment such as a dissolved cluster. Isochrone ages, tailored to measured metallicities, support earlier findings of a broad age mix in this group, ranging from ∼1 Gyr to as old as ∼8 Gyr. We performed an orbital frequency analysis in a Galactic potential that includes a rotating bar. Indeed, our sample stars fall onto thin resonances on corotation. Hence, our results support the idea that the HR 1614 MG is a resonantly perturbed disk feature, mustering a mélange of stars from different parent populations in the inner Galaxy.

Key words. stars: abundances – stars: kinematics and dynamics – galaxy: disk – galaxy: kinematics and dynamics – open clusters and associations: individual: HR 1614

1. Introduction

"Via lactea est omnis divisa in partes tres" – this dictum, loosely adapted from G. J. Caesar (58 BC), obviously purveys a hopelessly antiquated concept of a three-component (disk, bulge, and halo) Milky Way (MW) and its siblings (e.g., Kordopatis et al. 2013). Evidence has emerged that each of these is subdivided into thin and/or thick disks of various metallicities (e.g., Gilmore & Reid 1983; Kordopatis et al. 2013; Bensby et al. 2014), inner and/or outer halos displaying abundance gradients (e.g., Carollo et al. 2007; Koch et al. 2008), and a complicated bulge plus bar structure (e.g., Blitz & Spergel 1991; Stanek et al. 1997; McWilliam & Zoccali 2010; Wegg & Gerhard 2013; Kunder et al. 2020). Separation of all these is not straightforward and is further complicated by dynamical effects, dislocating stars and clusters from their birth radii, and redistributing angular momentum. This can lead to overlapping stellar populations (e.g., Koch et al. 2018; Gran et al. 2021) and various mixing effects, such as radial migration, blurring, or churning, all of which are essentially resonant effects due to non-axisymmetric perturbations (e.g., Sellwood & Binney 2002; Haywood 2008; Frankel et al. 2020). One class of objects attesting to the dynamic (co)evolution of these substructures is moving groups (MGs), i.e., ensembles of stars that are distinct in velocity and action space (Eggen 1958, 1965; Trick et al. 2021).

The HR 1614 MG was initially characterized as an old (∼2 Gyr), co-moving system in the survey of some 400 stars by Eggen (1971), who later noted the supersolar metallicities of the closest member (HR 1614≡Hip 23311) and 25 bright associates (Eggen 1978). Later, the group's age was revised upward to as high as ∼5 Gyr (Eggen 1992). Feltzing & Holmberg (2000) reexamined the HR 1614 group and its origin using various available data sets and a broad sampling of the phase space. In total, 44 stars were identified as possible members of the MG, with 60% being more metal-rich than the Sun, at a mean of ∼0.2 dex and an age back to Eggen's original assessment of ∼2 Gyr. Kushniruk et al. (2020) reviewed the group from a legion of surveys, resulting in a much larger sample of member candidates. Their ensuing isochrone fits revealed the presence of multiple stellar populations within the MG with ages between 2 and 8 Gyr and with a large spread in metallicity. Consequently, the origin of HR 1614 MG as a dissolved (open) star cluster was discarded (cf., Gagné et al. 2021).

Dynamically, its members stand out in the velocity space (U,V) at ∼(0, 60) km s^{-1} and within V±10 km s^{-1} of the

* This paper includes data gathered with the 6.5 m Magellan Telescopes located at Las Campanas Observatory, Chile.
** Corresponding author: andreas.koch@uni-heidelberg.de

Open Access article, published by EDP Sciences, under the terms of the Creative Commons Attribution License (https://creativecommons.org/licenses/by/4.0), which permits unrestricted use, distribution, and reproduction in any medium, provided the original work is properly cited.
This article is published in open access under the Subscribe to Open model. Subscribe to A&A to support open access publication.

reference star HR 1614. Given their propinquity and the tilt in the (U,V) space (see also Ramos et al. 2018), HR 1614 MG has been identified as part of the Hercules stream, which, in turn, constitutes a corotation resonance (CR) or outer Lindblad resonance (OLR) with the Galactic bar (Dehnen 2000; Hunt & Bovy 2018; D'Onghia & L. Aguerri 2020; Chiba et al. 2021; Li et al. 2025b,a).

In terms of a detailed chemical inventory, De Silva et al. (2007) conducted the first high-resolution spectroscopic study on 18 members of the group. Their results confirmed that the HR 1614 MG is a 2 Gyr old metal-rich system with [Fe/H] ∼0.25 dex. Additionally, chemical homogeneity due to the small scatter of only about 0.01 dex for several elements, coupled with the purported contemporaneous formation of the member stars, led to their conclusion that this MG originated from a dispersed star-forming event (see, also, Antoja et al. 2008). However, the main objective of the work of De Silva et al. (2007) was to perform a differential abundance study relative to the reference star HR 1614 in order to gauge abundance scatter with respect to measurement errors. Accordingly, only a brief discussion of the ages and kinematics of the stars was given, and the group's overall abundance patterns were not also placed in the broader picture of the underlying MW components. Similarly, while Kushniruk et al. (2020) identified a large number of candidate members with this MG, no detailed chemo-dynamic interpretation was carried out for these stars. In the present work, our aim is to fill this gap and to provide a detailed chemical abundance, age, and orbital analysis of a number of HR 1614 MG's member stars in order to connect it with the underlying MW components and to clarify its dynamic origin by resonant bar trapping.

This paper is organized as follows: in Sect. 2 we introduce the spectroscopic data. The abundance analysis is described in Sect. 3 and its results presented in Sect. 4. We derive stellar ages in Sect. 5, and in Sect. 6, the investigation of the group's dynamics is performed before concluding with a discussion in Sect. 7.

2. Observations and data reduction

Six stars believed to be part of the HR 1614 MG were selected from the sample of De Silva et al. (2007). Our choice of those stars was simply based on their brightness and observability. Our sample was observed with the Magellan Inamori Kyocera Echelle (MIKE) spectrograph at the 6.5 m Magellan 2 Clay telescope at the Las Campanas Observatory in Chile during the night of October 16, 2016. Each star was observed over four to five individual exposures with exposure times of 30 to 300 s each to facilitate cosmic ray removal. The seeing was overall unstable, varying between 2.0″ and 3.2″. We chose a slit width of 0.5″, which yielded a resolution power of around 40 000. The full wavelength range of the red arm of the spectrograph that we employ here is 4900–9500 Å. The S/N ratio for the bright targets ranges from 150 per pixel at shorter wavelengths to 300 per pixel in the red. The data reduction process followed standard procedures (Kelson et al. 2000; Kelson 2003), including bias correction, flat fielding, scattered light removal, spectral extraction, radial velocity correction (see Sect. 6), and continuum normalization (see Koch-Hansen et al. 2021 for a data set procured in the same night and processed in the identical manner).

3. Abundance analysis

We performed a standard abundance analysis that is based on both equivalent width (EW) measurements and spectral synthesis, where appropriate. For the major part, we restricted the EW determinations to the wavelength range between 5000 and 6600 Å; redward of 6600 Å, telluric absorption began to hamper the measurements, whereas the lines below ∼5000 Å became progressively blended, complicating the proper continuum placement in our metal-rich stars. We utilized the line list of Ruchti et al. (2013), which was constructed for stars of solar metallicity, and fitted Gaussian line profiles to the unsaturated lines with IRAF's *splot* task. We accounted for hyperfine splitting (chiefly for the Fe-peak elements), except for the weakest lines, using data from Johnson et al. (2006); Den Hartog et al. (2011); Mashonkina & Christlieb (2014); Lawler et al. (2015, 2019); Shi et al. (2018). A portion of our line list is given in Table 1.

Our study has 55 lines in common[1] with the analysis of De Silva et al. (2007) of Hip 23311. From these we find excellent agreement in our EW measurements with a mean deviation of a mere (0.8±1.3) mÅ with a 1σ-scatter of 9.8 mÅ. The corresponding fractional error is as low as (2±2)% and the two largest outliers, by ∼30 mÅ (or ∼30–40%), are a Ni and a Mg line.

The actual abundance derivation was carried out following the general methods used in, for example, Koch & McWilliam (2014), with the MOOG abundance code (Sneden 1973; 2019 version), building on the 72-layer, one-dimensional, plane-parallel grid of ATLAS atmospheres with solar-scaled opacity distributions, ODFNEW (Castelli & Kurucz 2003), under the assumption of local thermodynamic equilibrium (LTE) for all species.

3.1. Stellar parameters

Initial values for the stellar effective temperature, $T_{\rm eff}$, were obtained from the B_2 and V_1 Geneva photometry of Paunzen (2022), where we used the reddening maps and the extinction law of Schlafly & Finkbeiner (2011); Green et al. (2019) and applied the color-$T_{\rm eff}$-calibration of Ramírez & Meléndez (2005). An exception is Hip 23311, for which we resorted to the early photometry of Eggen (1977). For the surface gravity, $\log g$, we commenced with the canonical stellar relation from the stars' temperature, dereddened magnitude, distance (in turn based on Gaia parallax, Bailer-Jones et al. 2018), and mass. The microturbulent velocity, $v_{\rm mic}$, was initially set to 1.5 km s^{-1}, an initial mass of 0.8 $M_\odot$ was adopted (see also De Silva et al. 2007), and we started from Solar metallicities.

As the next step, $T_{\rm eff}$ was refined using about 100 iron lines and balancing the abundance with respect to the excitation potential. At the same time, $v_{\rm mic}$ was adapted until iron abundance did not show a trend with reduced width (RW) = $\log(\mathrm{EW}/\lambda)$. The stellar surface gravities were then derived by imposing ionization equilibrium between Fe I and Fe II lines. All parameters were thus iterated toward convergence, where we used the last derived iron abundance from the neutral lines as input to the next iteration's metallicity. In all this too strong and very weak lines with RWs above −4.5 and below −5.5 were culled from the analysis. The final stellar parameters used for the remainder of this study are listed in Table 2.

3.2. Differential analysis

A differential analysis relative to a reference star of similar parameters often proves useful in alleviating systematics in

[1] Unfortunately, De Silva et al. (2007) do not list any EWs for their other stars, but only one object, HR 1614, which constitutes the reference star for their differential analysis.

Table 1. Line list.

Species	λ_0 (Å)	EP (eV)	log gf	EW (mÅ)					
				Hip 11575	Hip 22336	Hip 22940	Hip 23311	Hip 26834	Hip 9353
26.0	5001.86	3.88	−0.010	97	100	130	106	134	90
26.0	5044.21	2.85	−2.038	81	76	93	144	88	75

Notes. Table 1 is available in its entirety in electronic form via CDS. A portion is shown here for guidance regarding content and form.

Table 2. Stellar parameters.

No.	ID (Hip)	V_0	$B_2 - V_1$	T_{eff}(spec) (K)	$T_{eff}(B_2 - V_1)$ (K)	log g	v_{mic} (km s^{-1})	[Fe/H] dex
1	11575	7.93	0.395	5900	5733	3.70	1.15	0.20
2	9353	5.81	0.349	6100	6279	3.95	1.10	0.32
3	22336	5.37	0.373	5900	6468	3.90	0.80	0.30
4	22940	8.29	0.524	5300	5188	4.33	0.40	0.17
5	23311	6.01	...	4850	...	4.23	0.90	0.13
6	26834	7.15	0.477	5575	5876	4.20	0.60	0.38

abundance determinations, mainly in terms of uncertain log gf values and adopted parameter scales (Fulbright et al. 2006; Koch & McWilliam 2008). We investigated this option for our study with a line-by-line differential analysis relative to the Sun, exemplified for star Hip 22336, with its parameters closest to the Sun; to this end, we employed the Solar line list from Fulbright et al. (2006) and measured the same lines in the target star. The Solar parameters were adopted from Fulbright et al. (2006), namely (T_{eff}, log g, v_{mic})$_\odot$ = (5770 K, 4.44 dex, 0.93 km s^{-1}). In order to recover excitation and RW balances of the line-by-line differences $\epsilon_* - \epsilon_\odot$, the "absolute" parameters for this star (see above and Table 2) had to be altered, albeit to within their uncertainties. The resulting differential parameters for Hip 22336 are thus (T_{eff}, log g, v_{mic})$_*$ = (5930 K, 4.12 dex, 1.10 km s^{-1}). Similarly, we find a slightly lower differential Fe-abundance, at 0.23±0.01 dex, for both neutral and ionized species. Given the broad mix of parameters across the sample and since the results are in broad agreement, we do not pursue this method any further.

3.3. Error analysis

An order of magnitude for the statistical 1σ-error on T_{eff} and v_{mic} was estimated by adjusting these parameters until the slopes of the Fe-abundance were still within the 1σ-scatter in the excitation potential and RW diagrams, respectively. This yields formal uncertainties of ±30 K and ±0.1 km s^{-1}. Moreover, we note that the mean deviation between the spectroscopic and photometric temperatures is 33±115 K, which alters the abundance results only marginally. Although agreeing very well on average, the 1σ-scatter in comparison with the T_{eff}-scale of De Silva et al. (2007) is larger, at 160 K. In the following, we adopt a representative temperature uncertainty of 100 K in our measurements. Likewise, the star-by-star comparison with the literature values reveals a fair agreement between the gravities, with the literature values being higher by 0.25 dex at a 1σ-scatter of 0.14 dex. Finally, the microturbulent velocities are broadly in agreement with those of De Silva et al. (2007), with a spread of 0.19 km s^{-1}.

The main sources of statistical abundance errors are from the measurements of EWs per continuum placement and the number of lines used, N. Therefore, in our following results we state the statistical errors via the standard deviation of the abundance values and the number of lines used.

Systematic errors, in turn, were derived by varying every stellar parameter about its uncertainty (estimated above) individually, computing new abundances, and noting the difference to the unperturbed values. Furthermore, an additional analysis with α-enhanced model atmospheres (AODFNEW) was performed, thereby mimicking a halo-like [α/Fe] ratio of 0.4 dex, which reflects our ab initio ignorance of the stars' α-abundances. The final systematic error is calculated from the squared sum of those differences. However, this should be considered as an upper limit, since cross-terms between stellar parameters were not taken into account (McWilliam et al. 1995). The results are given in Table A.1 in the appendix, for the example of the target star Hip 11575.

4. Abundance results

The results of the chemical abundance analysis for the entire sample are presented in Table A.2 in the appendix, where the abundances of ionized species are given relative to ionized iron, and neutral species relative to Fe I. Throughout, we adopted the Solar abundances from Asplund et al. (2009). In the following, our measurements are placed in context with the Galactic thin and thick disks, with the data from the literature indicated in the respective captions (Figs. 1–7). We also note that all abundances in the literature are reported in LTE unless otherwise noted.

4.1. Iron

All in all, the iron abundance is supersolar for all stars with a mean of 0.25 dex and a 1σ-scatter of 0.09 dex. This lies well above the typical spread in a given cluster or the formerly coherent and now defunct structure, which tend to have intrinsic spreads well below 0.02 dex for most elements (Sinha et al. 2024), and again argues against the HR1614 MG being a dissolved star cluster (Kushniruk et al. 2020; Li et al. 2025b). For our stars, the values are in excellent agreement to within 0.10 dex with those of De Silva et al. (2007), differing only by ∼0.14 dex for the eponymous HR 1614 (≡Hip 23311). The latter star had

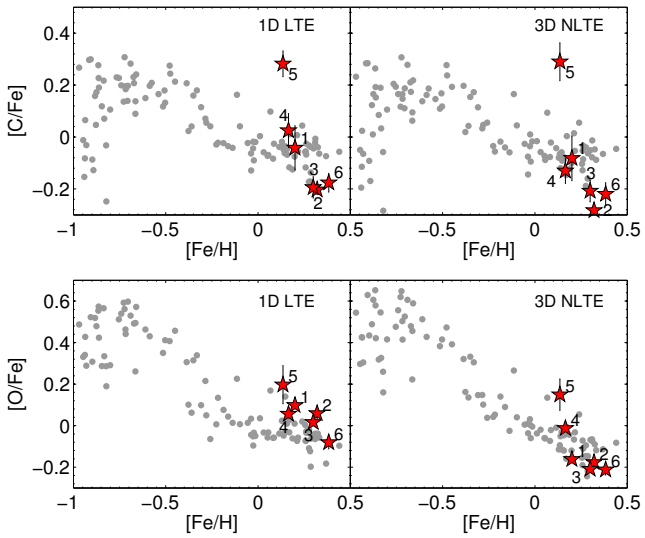


Fig. 1. Carbon (top panels) and oxygen (bottom) abundances in 1D LTE and after applying NLTE 3D corrections. The corrections and literature data are from Amarsi et al. (2019). The most metal-poor star of our sample, Hip 23311, has an elevated ratio, in line with a thick disk origin. In this and the following figures, numbers encode the target stars as follows: 1: Hip 11575; 2: Hip 9353; 3: Hip 22336; 4: Hip 22940; 5: Hip 23311; 6: Hip 26834.

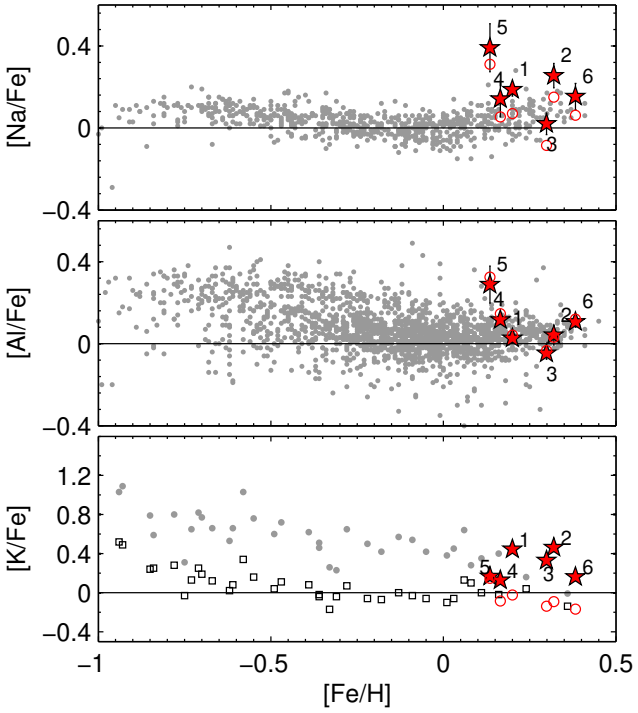


Fig. 2. Abundance ratios of the light elements Na, Al, and K for our target stars (red star symbols) and literature data (gray dots), which have been taken from Takeda et al. (2002), Bensby et al. (2014), and Delgado Mena et al. (2017). We also show NLTE-corrected values (open circles) with corrections from Lind et al. (2011), Nordlander & Lind (2017), and Takeda et al. (2002). The bottom panel also includes NLTE abundances for the disk stars (black open squares) as provided by Takeda et al. (2002).

been analyzed by Antipova & Boyarchuk (2016), who found it to be rather "anomalous" in the sense of its stellar parameters strongly differing between photometry and spectroscopy, also noting several apparent abundance anomalies. This finding led those authors to conclude that Hip 23311 is a red dwarf with strong, solar-like atmospheric activity. We also note that, per construction, ionization balance is fulfilled in the stars, with a mean [Fe I/II] ratio of 0.00±0.01 dex.

4.2. Light elements: C, O, Na, Al, K

We determined the carbon abundance in all six stars from the two atomic lines at 5380 and 6587 Å. Corrections for non-LTE (NLTE) were interpolated from Amarsi et al. (2019) and are typically less than 0.1 dex. Our stars lie, within the uncertainties, on the roughly flat trend delineated by similar MW field stars at Solar to supersolar metallicities. Here, and in many other elements discussed below, Hip 23311 is an outlier with a carbon-enhancement of ~0.3 dex.

Oxygen abundances are based on the triplet lines around 7774 Å. In contrast to carbon, the [O/Fe] ratios are prone to large NLTE corrections. In Fig. 1, we show our results together with the uncorrected (left panels) disk star sample of Amarsi et al. (2019, and references therein) and their sample after applying their 3D-NLTE corrections (right panel; see also Sitnova et al. 2013; Steffen et al. 2015). In either case, the HR 1614 MG stars are fully consistent with the thin disk trend, even tighter in the corrected case, with the exception of Hip 23311, which shows an enhancement of [O/Fe]~0.2 dex. This value is in agreement with the higher-α sequence that is populated by thick disk stars (e.g., Franchini et al. 2021). We note that despite this star's still relatively high metallicity of ~0.1 dex, it is the most "metal-poor" object in our sample.

Fig. 2 shows the abundance ratios of the remaining light elements with data from the literature for MW disk stars, as indicated in the caption. The Na abundances were derived from line pairs at ~5682 and ~6154 Å. Most stars follow the disk trends for metal-rich stars, even more so after adjusting the abundances by ~0.1 dex for each star to account for the NLTE corrections implied by Lind et al. (2011). We determined the aluminium abundances of our stars from the moderately strong 6696, 6698, and 7835 Å lines and determined small NLTE corrections (Nordlander & Lind 2017). For potassium, only one line at 7698 Å was usable, which was not hampered by the overlapping telluric A band. Also, for K, our sample is fully in line with disk stars from the literature (Takeda et al. 2002). The latter work's NLTE corrections lower the [K/Fe] ratios to the Solar level over a broad range in metallicity; similar results are achieved when using the corrections of Reggiani et al. (2019). In all these elements, but K, Hip 23311 stands out because it has enhanced abundance ratios.

4.3. α-elements: Mg, Si, S, Ca, Ti

The abundance results for the α-elements are chiefly based on standard line lists and procedures as in our previous work. The element sulfur, less studied, was analyzed by synthesizing the M6 and M8 multiplets, using line data from Caffau et al. (2005). Fig. 3 shows our abundance ratios on the trends for MW thin and thick disk stars, with reference data from Caffau et al. (2005) and Bensby et al. (2014). For completeness, we investigate the effects of NLTE on all elements in this group using line-by-line data for Mg (Bergemann et al. 2017), Si (Bergemann et al. 2013), Ca (Mashonkina et al. 2007), and Ti (Bergemann 2011). The corrections for sulfur are small in Solar type stars

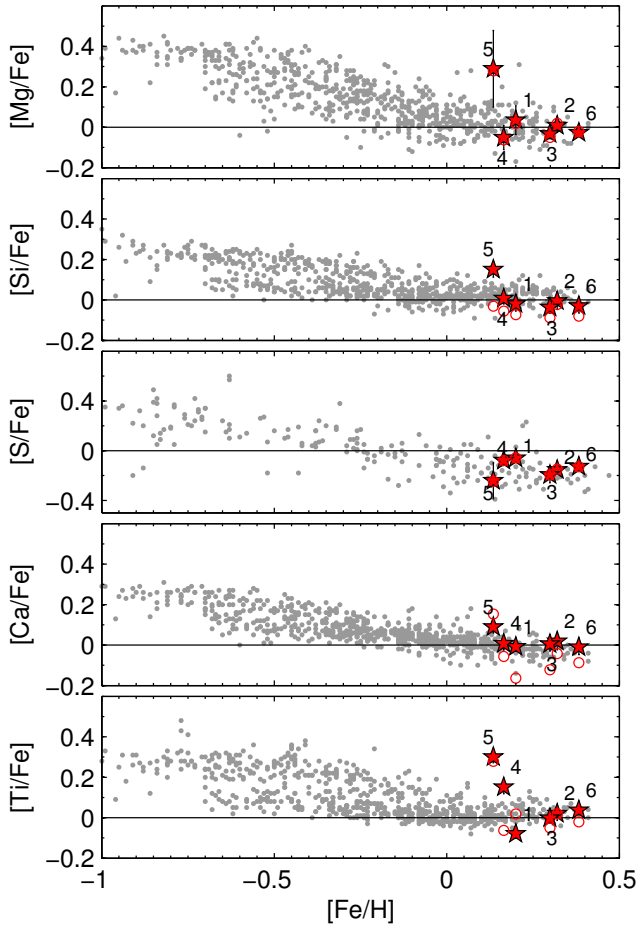


Fig. 3. [X/Fe] for various α-elements of the HR 1614 MG stars (red symbols) compared to the MW disks (gray dots), using data from Bensby et al. (2014) and Caffau et al. (2005) for sulfur. All [X/Fe] and [Fe/H] are LTE values, while red open circles include NLTE corrections in the elements' abundances for our six stars.

(Amarsi et al. 2025), but also strongly hinge on the treatment of the cross section of hydrogen collisions (Koch & Caffau 2011). All NLTE-corrected values are indicated as open red circles in Fig. 3 and the following figures.

One point to note are the error bars for Mg (top panel of Fig. 3). Magnesium lines are typically very strong, especially those near 5528 Å and 5711 Å. In order to assess the risk of possible saturation, we synthesized these two lines, noting the effect that varying abundances had on the line fit. Thus, the poorest result was obtained for the most metal-rich star in our sample, Hip 26834. Overall, the [α/Fe] ratios agree well with the underlying disk trends, again with the exception of Hip 23311. Similarly, the largest scatter over the metallicity range covered by our small sample is seen for Ti (bottom panel of Fig. 3). We note, however, that this is again driven by the two most metal-poor stars in our sample that show [Ti/Fe] ratios enhanced to 0.3 and 0.2 dex above the otherwise Solar ratios in our stars.

In order to emphasize the contrast in our data, we show in Fig. 4 the straight average over the four main α-elements Mg, Si, Ca, and Ti, disregarding differences in their nucleosynthetic formation details due to their hydrostatic or explosive nature (Woosley & Weaver 1995; Venn et al. 2004). All but one star match the literature values for metal-rich thin disk stars. As before, it is Hip 23311 (and, to a lesser extent, Hip 26384) that deviates from the Solar (averaged) abundance ratios and instead

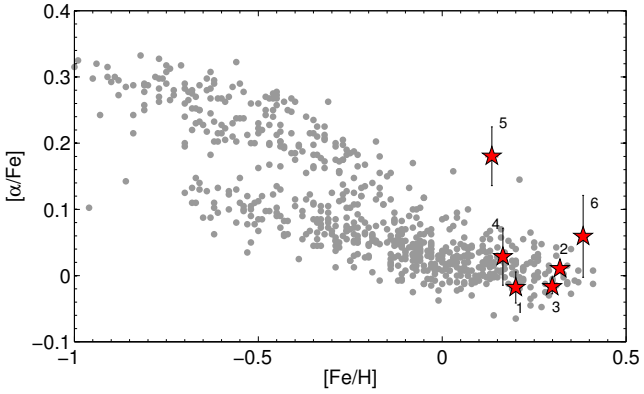


Fig. 4. Mean [α/Fe] ratio of the elements Mg, Si, Ca, and Ti in LTE; oxygen and sulfur were not included in this average. Literature data are from Bensby et al. (2014). Symbols are as in Fig. 3.

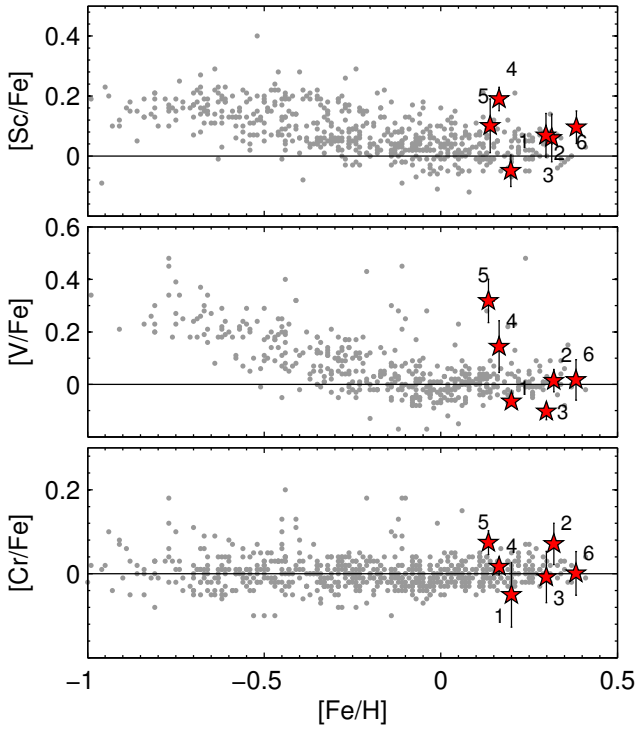


Fig. 5. Same as Fig. 3, but for the Fe-peak elements Sc, V, and Cr. Literature data are from Bensby et al. (2014) and Battistini & Bensby (2015).

follows the rising trend of the higher-α stars in the thick disk. Thus, our chemical evidence so far shows that there is a mixed origin of the HR 1614 MG of thin and thick disk stars. Indeed, large local samples show chemically thick disk stars among the kinematically thin disk population, and vice versa (e.g., Bensby et al. 2014; McWilliam 2016; and Sect. 6.2). In this regard, Hip 23311 and Hip 26384 are not unusual. However, the iron abundance for Hip 23311 in our work is lower by ~0.2 dex compared to the value reported by De Silva et al. (2007).

4.4. Fe-peak elements: Sc, V, Cr, Mn, Co, Ni, Cu

In Figs. 5 and 6, we show our results for the Fe-peak results compared to data from the literature as indicated. None of Sc, V, and Ni were corrected for departures from LTE

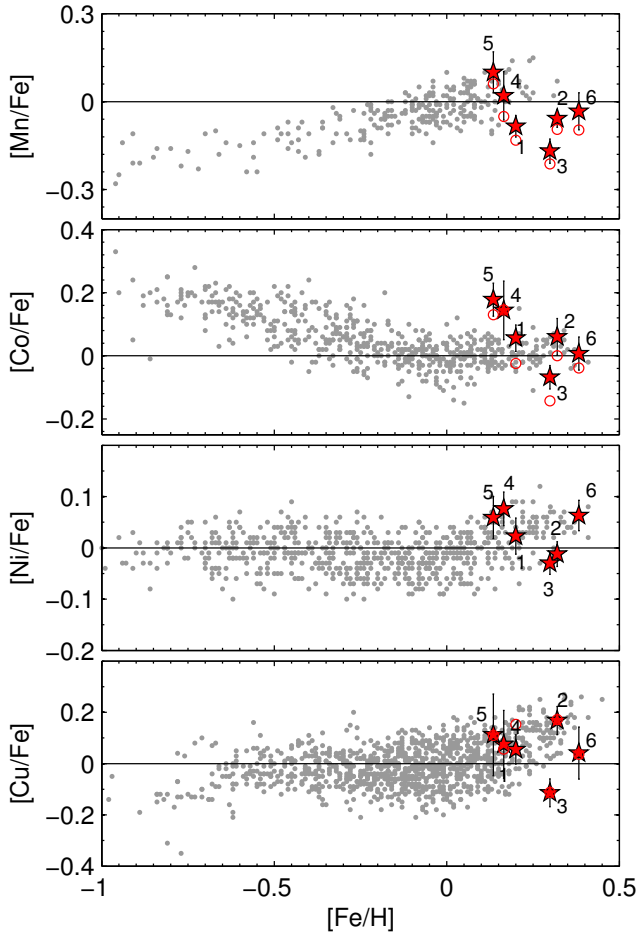


Fig. 6. Same as Fig. 3, but for the remaining Fe-peak elements. The reference samples were taken from Mishenina et al. (2015), Battistini & Bensby (2015), Bensby et al. (2014), and Delgado Mena et al. (2017). Red circles denote the values corrected for NLTE-effects, using data from Bergemann & Gehren (2008) for Mn, Bergemann et al. (2010) for Co, and Caliskan et al. (2025) for Cu.

(Nissen et al. 2024). The elements Sc, V, and Cr exhibit trends that are in line with the underlying MW distribution. Here, the [Sc/Fe] ratios are very close to typical MW stars for their [Fe/H]. Although Type Ia Supernovae (SNe Ia; including those at sub-Chandrasekhar mass) tend to underproduce Sc in the thick disk, the [Sc/Fe] ratios are enhanced, often in lockstep with the elevated α-levels found in systems with enhanced SNe II ejecta (e.g., Prochaska et al. 2000). Thus, the solar-like [Sc/Fe] ratios in the HR 1614 MG stars suggest a similar SNe II/Ia ratio as in the Solar neighborhood. The same trend is visible for [V/Fe], albeit noisier, which is mainly driven by Hip 23311, but a similar scatter is seen in the values reported for disk stars in the literature.

For Cr, we applied NLTE corrections for those lines with available data (Bergemann & Cescutti 2010). However, those corrections largely average out among the used lines for our targets, and the only discernible result is a slightly increased line-to-line scatter for each star.

At their supersolar metallicities, the [Mn/Fe] ratios of our stars start turning over from the Galactic trend of increasing Mn-abundance with increasing [Fe/H] (Mishenina et al. 2015) toward mostly sub-Solar ratios (top panel of Fig. 6). Here, we also show NLTE-corrected values from the line-by-line prescriptions of Bergemann & Gehren (2008), which lower the Mn abundance ratio by ∼0.05 dex.

In the plot for [Co/Fe], one sees the same behavior as for the other Fe-peak elements in comparison with Galactic stars. As for other elements, Hip 23311 stands out with its elevated abundance, while Hip 9353 also displays an enhancement, albeit with a larger error bar due to the use of only two lines with significantly differing EWs. For all measurements, we have applied the NLTE corrections from Bergemann et al. (2010), on the order of 0.05–0.1 dex, with the corrected values indicated in Fig. 6.

It is noticeable that the Mn/Fe, Co/Fe (and possibly Zr/Fe and V/Fe) ratios show downward trends with increasing [Fe/H], even if Hip 23311 was removed from the reasoning. This is unlikely to be a measurement artifact, since proper treatment of the hyperfine splitting was applied, and, despite Cu I also suffering strongly from that effect, [Cu/Fe] is reasonably well behaved in our sample. This would suggest that this trend in our sample of metal-rich stars cannot be due to different dilutions of SNe ejecta with different amounts of pure hydrogen. Rather, it indicates a change in the average yields with increasing metallicity in a chemically evolving system.

Our work provides the first measurements of Cu in the stars of this MG. To this end, three useful lines (at 5105, 5700, and 5782 Å) were present in the spectra, with EWs typically on the order of ∼100 Å. To determine the [Cu/Fe] ratio, we resorted to synthesizing those lines. Their NLTE corrections are small (Caliskan et al. 2025) and barely discernible in Fig. 6. At their slightly supersolar values, all stars (except one, Hip 22336) nicely follow the trend outlined by Galactic disk stars (Mishenina et al. 2011; Delgado Mena et al. 2017). We note that the lower-Cu star Hip 22336 also shows the lowest [Mn/Fe] and [Co/Fe] ratios in our sample. As McWilliam et al. (2003) and McWilliam & Smecker-Hane (2005) showed, Cu depletions are followed by deficiencies in [Mn/Fe] as well, which can be explained by low-metallicity SNe Ia and metallicity-dependent (SNe Ia and SNe II) yields. However, those studies focused on the Sagittarius (Sgr) dwarf galaxy and neither our Cu- or Mn depletions are as pronounced as in the lower-metallicity Sgr-stars.

Finally, Ni invariably traces iron, as expected given its lockstep production in regular Chandrasekhar-mass SNe Ia (e.g., Woosley & Weaver 1995; Kobayashi et al. 2020). Li et al. (2025b) used abundances from the APOGEE and GALAH surveys to argue for a "low alpha thin disc" HR 1614 subgroup to be enhanced in Na, Al, V, and Ni, while the enhancements we find here are mainly pertaining to those stars with a more likely thick disk origin.

4.5. Heavy elements: Y, Zr, Ba, La, Eu

In Fig. 7, we show the neutron-capture elements we measured in our stars. The [Y/Fe] ratio of our stars, derived from spectral synthesis, is perfectly in line with the distribution in the disk, showcasing its origin in a standard, slow (*s*-) neutron capture process (e.g., Busso et al. 1999; Tautvaišienė et al. 2021). The usual contender for outlying abundance is Hip 23311 with an overabundance of ∼0.4 dex. This is also observed for Zr, where we find, however, that the three most metal-rich stars are depleted with respect to the remainder of metal-rich disk stars. We assessed NLTE-corrections on Zr by comparison with Zhao et al. (2016) and estimate departures of ∼0.1 dex only for the three warmer stars in our sample, with null corrections otherwise.

The Ba-abundances in our stars are in very good agreement with the Ba-determination of De Silva et al. (2007) and with those in metal-rich disk stars. Also, the EWs for star Hip 23311 agree excellently with their measurements with a mean deviation

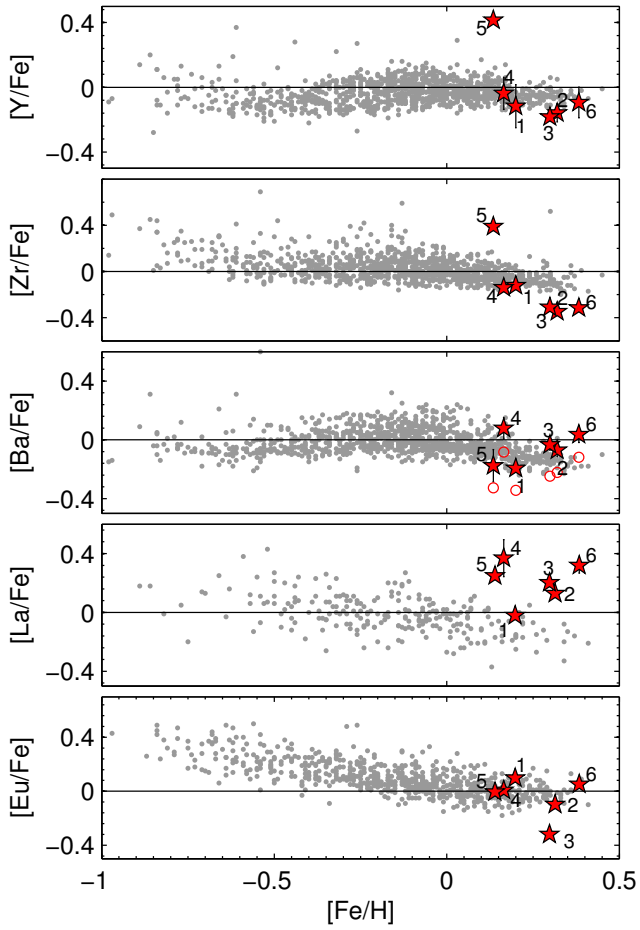


Fig. 7. Same as Fig. 3, but for neutron-capture elements. Reference data are from Koch & Edvardsson (2002), Bensby et al. (2014), and Delgado Mena et al. (2017).

of −2.2 ± 2.9 mÅ for the three lines in common. For reference, we indicate in Fig. 7 Ba-values corrected for NLTE by using the line-by-line departures given by Gallagher et al. (2020), albeit for the Sun. In turn, a broad range in [La/Fe] ratios is found from rather weak lines in our stars, with values lying above the disk trend by ∼0.4 dex.

Finally, the Eu abundances align very well with the results of De Silva et al. (2007), despite being based on a single line at 6645 Å. NLTE-corrections are very small in the parameter space of $T_{\rm eff}$ and [Fe/H] of our stars (Zhao et al. 2016) and we do not show them any further in Fig. 7. In particular, five of our six stars are fully consistent with the MW disk, while Hip 22336 is depleted by ∼ − 0.3 dex. This is particularly noteworthy, as this star was already shown to have systematically lower abundances of Mn, Co, and Cu compared to the remainder of our sample.

Our results indicate a high *hs*/*ls*-ratio in excess of 0.8 dex (taken here as the average of Ba and La relative to Y and Zr; listed in Table A.2), which normally is indicative for *s*-processing in metal-poor asymptotic giant branch (AGB) stars (e.g., Busso et al. 1999), due to the larger ratio of neutrons per Fe-seed nucleus driving the synthesized elements to high mass numbers. However, in our sample, we see high *hs*/*ls*-ratios at high metallicity, contrary to this expectation. This may be due to a higher total neutron exposure in the polluting AGB stars. The usual deviation from this trend is Hip 23311 with a *hs*/*ls*-ratio well below zero.

4.6. Intrinsic abundance spreads

Smith (1983) used DDO photometry for 19 of the originally confirmed (26) metal-rich member stars of the HR 1614 MG and discovered anomalies in the sense of a large number of CN-rich stars. On the one hand, this finding cemented the original proposition of Eggen (1978) of the physical association of the stars of the purported group. However, Smith (1983) argued from the then-available kinematics that those stars cover a broad range of orbits, with peri- and apocenter radii of 6.5–10.4 kpc, and therefore must have formed in a region of larger extent than a typical (open) cluster. Reasoning from their CN-enhancements within the framework of a Galactic abundance gradient in the old disk, they stated that spatial and temporal heterogeneities are likely to occur in the region within the disk where those stars have formed.

In order to quantify the intrinsic abundance spread for each element, we follow the probabilistic approach of Piatti & Koch (2018, in turn based on Walker et al. 2006). The resulting scatter σ_0, which also accounts for measurement errors, is listed in the last column of Table A.2 in the appendix. Here, the scatter in Fe-abundance amounts to 0.09 dex alone, which is significant at the 3σ-level. The highest spread of 0.32 dex is found for Ti II, while it is lower for neutral Ti and thus could indicate a systematic effect in the measurements or NLTE effects. Similarly large spreads of 0.25 dex are seen for Zr and C. The lowest value, in turn, is only found for the α-elements S and Ca, which, at a mere 0.02±0.02 dex each, are consistent with a homogeneous origin.

In conclusion, 21 out of the 27 abundances we measured show intrinsic spreads that are significantly above zero at least at the 2σ level. This is in contrast to De Silva et al. (2007), who found a very low scatter in most elements of their sample of 18 group members. They stated an intrinsic scatter around 0.01–0.03 dex (at the 80% confidence level; CL) for most of the studied elements. Coupled with the coetaneous ages of the group stated by De Silva et al. (2007), this chemical homogeneity was taken as evidence for the MG originating in an unperturbed, dispersed star-formation event. Our finding of significant intrinsic abundance spreads also bolsters previous results that the HR 1614 MG is not a dissolved open cluster (Kushniruk et al. 2020): in their sample of 26 open clusters, Sinha et al. (2024) determined very low spreads below <0.02 dex (at the 3σ-level) for most of the (20) measured elements of their APOGEE cluster sample, although a different metric was used from ours. Exceptions to this lack of dispersion were found mainly for the weak-lined neutron-capture elements, resulting in larger spreads of ∼0.2 dex.

The large abundance spreads seen in our analysis rather argue in favor of dynamical mixing events bringing together stars from various environments, in particular, as MW stars tend toward chemical homogeneity to within ∼0.02 dex at a given galactocentric radius (Ness et al. 2022). As we also reason in Sect. 6, at least part of our sample has a thick disk origin.

5. Ages

While Feltzing & Holmberg (2000) obtained a single age of ∼2 Gyr with the possibility of some spread for the HR 1614 MG as an ensemble, Kushniruk et al. (2020) derived ages from an unprecedentedly large number of $O(10^4)$ stars using Gaia photometry and photometric metallicities from the SkyMapper survey (Keller et al. 2007), but no comments on individual stars were made. Despite our smaller sample size, we are in the fortunate situation of having precise and accurate abundance

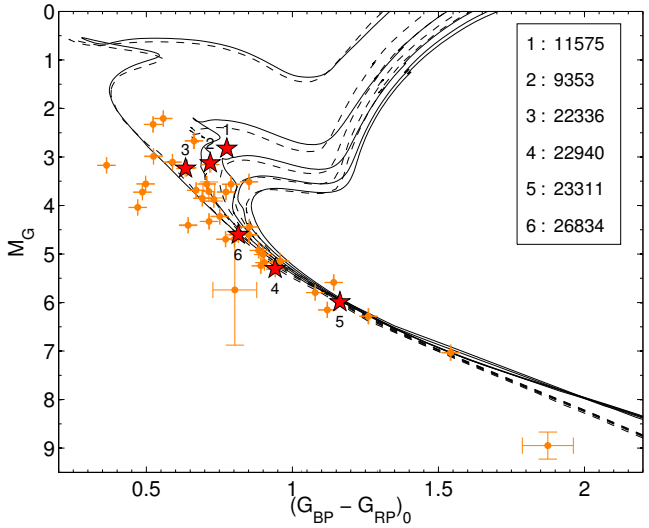


Fig. 8. CMD of our target stars (red symbols) and those of Feltzing & Holmberg (2000, orange points) with the set of Dartmouth isochrones (Dotter et al. 2008; solid lines) and the rotating PARSEC isochrones (Nguyen et al. 2022; dashed lines) used for age estimates. While each star was fit with an isochrone of its individual metallicity, we show here an exemplary set of [M/H]=0.2 dex for ages of 1 to 9 Gyr in steps of 2 Gyr. As before, number labels refer to Hip numbers.

measurements that we use as input for fitting isochrones in an effort to derive individual stellar ages of our targeted group members.

In practice, we estimated ages via fitting the suite of Dartmouth isochrones[2] (Dotter et al. 2008), tailored to each star's individual metallicity, to the targets' location in a color-magnitude diagram (CMD) from Gaia photometry (Gaia Collaboration 2023, see Fig. 8). To this end, we employed distances and extinctions from Bailer-Jones et al. (2018) and Queiroz et al. (2018), and the extinction law of Yang et al. (2023).

As Fig. 8 indicates, three stars of our sample lie below the age-sensitive main-sequence turn-off and the isochrone fits merely return the oldest age used in the grid. For the other MG member stars, we obtain ages of 3.0±0.8 Gyr (Hip 11575), 2.8±0.4 Gyr (Hip 9353), and 4.4±0.7 Gyr (Hip 22336), respectively. The age errors stated were based on the photometric and parallax errors provided by the Gaia Collaboration (2023), and accounting for a metallicity uncertainty of ±0.1 dex. This leads to relative age errors on the order of 15–30% for the three reliable measurements.[3]

The range of possible ages of the HR 1614 MG we find emphasizes the possibility that members of this group can indeed be older and diverse stars, which is, in fact, in line with Hufnagel & Smith (1994), who found from chromospheric activity indicators that their analyzed stars in this MG are older than 3 Gyr. Previous estimates from canonical isochrone fitting, as we have employed here, have placed the age of this moving group at a slightly younger age of around 2 Gyr (Feltzing & Holmberg 2000), although Kushniruk et al. (2020) assert that a broad age

[2] These do not account for stellar rotation as our stars, at M≲1.3 $M_\odot$ (De Silva et al. 2007), are likely not strongly affected by this effect. Switching to the PARSEC isochrones that include rotation above ∼1 $M_\odot$ (Nguyen et al. 2022) has little impact on the ages derived here.

[3] We also employed the [Y/Mg] ratio as a chemical clock, using the calibration of Casali et al. (2020) to estimate ages of ∼1.4±0.8 dex for Hip 11575, 9353, and 22336, and 2.4±1.0 Gyr for Hip 26384, while for the other two, no physically meaningful values could be determined.

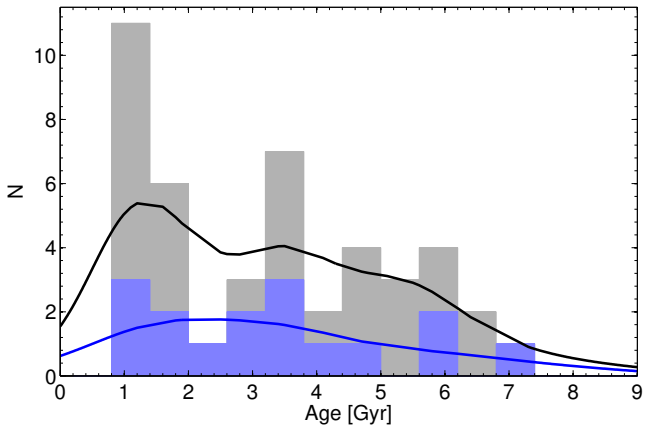


Fig. 9. Histogram of ages derived from the sample of Feltzing & Holmberg (2000). The entire sample is shown as gray-shaded, while stars on the upper, more age-sensitive color-magnitude distribution are highlighted in blue. Solid lines show the respective error-weighted distributions.

range with prominent peaks around ∼2 and ∼8 Gyr indicate stars of a multifarious disk origin within the MG.

We therefore summon up the same exercise as above for the bona fide sample from Feltzing & Holmberg (2000), bearing in mind that their metallicity scale from Strömgren photometry and, for a handful stars, [Fe/H] from spectroscopic measurements from the literature are be different from ours, which poses a possible cause for systematic offsets. As before, we obtained those stars' photometry and parallaxes from the Gaia Collaboration (2023). The resulting age distribution is shown in Fig. 9.

As a considerable fraction of the stars lie below the respective turn-offs on the rather age-insensitive main sequence, we also constructed the same histogram for stars brighter than the (arbitrary) limit of $M_G < 4$ mag. It becomes immediately obvious, as also implied by the color-magnitude distribution of the sample, that the stars in this group span a large range of ages. The strong peak at the youngest ages (most strongly visible in the full distribution shown in gray in Fig. 9) can be attributed to the limit of our fitted isochrone grid and therefore represents an artifact. Nonetheless, each distribution shown in Fig. 9 displays clear maxima of up to 2 and at ∼3.5 Gyr. Further peaks at 5 Gyr and above ∼6.5 Gyr are also discernible, although less pronounced.

Most likely is a coincidence of this dynamical group with the interaction with the Galactic bar, which we explore in greater detail in the next section. The bar may have already formed early on with a steep cessation in star formation as, for example, found from studies of its supermetal-rich populations (Nepal et al. 2024; see also Sanders et al. 2024). An age of the bar itself that is too young is dynamically not feasible or likely (e.g., Debattista et al. 2019; Anderson et al. 2024).

6. Dynamics

Radial velocities were derived using a cross-correlation of the spectra against a synthetic spectrum using IRAF's *fxcor* task (Tonry & Davis 1979), where we restricted our measurements to the less-blended wavelength region of 5700–6400 Å. The resulting velocity uncertainties are on the order of 0.1 km s^{-1}. Our derived velocities are in good agreement with those of the literature (De Silva et al. 2007; Feltzing & Holmberg 2000,

and references therein), with an average difference of −0.2 km s^{-1}. Slightly larger deviations are only found for Hip 23311 and Hip 26834, for both of which Feltzing & Holmberg (2000) reported velocities larger by 6–7 km s^{-1} than our and De Silva's (2007) values. Furthermore, proper motions were taken from the third data release of Gaia (Gaia Collaboration 2023), along with distances, extinctions, and reddening corrections from Bailer-Jones et al. (2018) and Queiroz et al. (2018). The observed and derived properties of our sample are detailed in Table B.1 in the appendix.

6.1. Orbit integration

With a bar resonance being a strong contender for having stirred up stars into their dynamical coherence, particular care has to be applied to the potential of that particular MW component. Thus, we used the `AGAMA` package (Vasiliev 2019) together with the MW potential model of Hunter et al. (2024). This model provides a self-consistent non-axisymmetric description of the inner Galaxy. The potential includes the central black hole, the nuclear star cluster, the nuclear stellar disk, and the dark halo in an axisymmetric multipole component, while the bar, thin and thick stellar disks, and the gas disks are represented by a triaxial `CylSpline`[4] component.

The bar rotates clockwise in the Galactocentric (x, y) plane, i.e., in the same sense as Galactic disk rotation in the adopted AGAMA convention; throughout this work we quote the absolute value of the pattern speed, with a pattern speed of $\Omega_{\rm bar}$ = 37 km s^{-1} kpc^{-1} oriented at an angle of 27° with respect to the Sun–Galactic-center line.

For the analysis presented here we used the rotating version of the model without spiral arms. For comparison, we also tested the corresponding rotating model that includes spiral arms. The optional spiral component in the Hunter et al. model is implemented as a separate, more slowly rotating `CylSpline` perturbation. It is constructed from two phase-shifted $m = 2$ logarithmic spiral sets and represented with azimuthal harmonics up to $m_{\rm max} = 8$. For the six stars, the inclusion of the spiral component only has an insignificant impact on the derived parameters: the pericenters change by at most 0.032 kpc, apocenters by 0.072 kpc, eccentricities by 0.007, and $Z_{\rm max}$ by 0.003 kpc. These correspond to relative changes below 0.9% for the orbital radii and less than 2.5% for $Z_{\rm max}$.

For each star, the observed phase-space coordinates were transformed into a galactocentric frame assuming R_0 = 8.179 kpc, $z_\odot$ = 20.8 pc, and a solar velocity of $(U, V, W)_\odot$ = (11.1, 245.0, 7.25) km s^{-1}. The resulting Cartesian coordinates and velocities were then rotated into the bar frame before orbit integration. Orbits were integrated for 5 Gyr using the rotating Hunter et al. potential and sampled with 10^5 trajectory points. From the resulting trajectories we derived pericenters, apocenters, eccentricities, maximum vertical excursions, angular momenta, and energies. In addition, we computed the fundamental orbital frequencies in both the inertial and bar-rotating frames.

Uncertainties in the derived orbital parameters were quantified with a Monte Carlo sampling procedure. For each star, we constructed a covariance matrix from the measured radial velocity, distance, and proper motions (μ_α, μ_δ), including the variances of the individual quantities and the covariance between the two proper motion components. We then drew 1000 Monte Carlo realizations per star. For each realization, the full coordinate transformation, rotation into the bar frame, orbit integration, and frequency determination were repeated. The reported orbital quantities are the median values of the Monte Carlo realizations, while the 16th and 84th percentiles are used as a robust 68% uncertainty interval.

6.2. Orbital parameters

The estimated orbital parameters of our stars and their uncertainties are listed in Table B.1, and illustrations of the orbits in the rest frame of the bar are shown in Fig. , each in the appendix. All six orbits remain confined close to the Galactic mid-plane in the rotating potential. The maximum vertical excursions span $Z_{\rm max}$ = 0.036–0.238 kpc. Hip 22336 reaches the largest height above the plane, $Z_{\rm max}$ = 0.238 kpc, whereas Hip 22940 and Hip 23311 remain very close to the plane, with $Z_{\rm max}$ = 0.036 and 0.053 kpc, respectively.

The overall structure of the orbits is remarkably homogeneous. The apocenters are clustered tightly around $R_{\rm Apo}$ = 8.53 kpc, with a full range of only 0.17 kpc, while the pericenters are found around $R_{\rm Peri}$ = 3.64 kpc, spanning 0.36 kpc. This yields eccentricities in the narrow interval $e \simeq 0.39$–0.44 for all six stars. The most eccentric orbit is that of Hip 22336, with e = 0.436, which is also the star with the smallest pericenter, $R_{\rm Peri}$ = 3.37 kpc. The orbital periods about the Z-axis are also nearly identical, at $P_z \simeq 0.16$–0.17 Gyr. We note that this coincides with the period of the bar for our assumed pattern speed of $\Omega_{\rm bar}$ = 37 km s^{-1} kpc^{-1}, so that in the rotating frame of the bar the Jacobi integral ($E_{\rm J}$, also listed in Tab. B.1) is approximately conserved and all six stars occupy a very narrow range in $E_{\rm J}$.

The angular momenta and present-day azimuthal velocities are also very similar across the sample. In the sign convention of the present integration, the prograde orbits have positive angular momenta, with $|L_z| = 1.41$–1.55×10^3 kpc km s^{-1}. Hip 22336 is the kinematically warmest object in the sample, with the lowest $|L_z|$, the lowest $|V_\phi|$, the largest vertical excursion, and the largest eccentricity.

In the local velocity plane (Fig. 10), the MG members also form a compact, though tilted sequence at $V_{\rm LSR} \sim -50$ km s^{-1} that follows and slightly extends the group as selected by Feltzing & Holmberg (2000). The Toomre diagram (Fig. 11) reinforces the formation picture of the HR 1614 MG. For each star, this shows its Galactic rotational component ($V_{\rm LSR}$) against the vertical and radial deviations thereof, i.e., $T \equiv \sqrt{U_{\rm LSR}^2 + W_{\rm LSR}^2}$. Five of our target stars lie in the thin-disk locus with modest T and mildly lagging $V_{\rm LSR}$. Hip 22336 is a clear kinematic outlier, placing it in the transition band toward the thick disk. This behavior is consistent with its larger $Z_{\rm max}$, lower L_z, and higher $|U_{\rm LSR}|$. Overall, the distribution of our analyzed stars overlaps the locus of the literature HR 1614 MG members from Feltzing & Holmberg (2000), yet Hip 22336 sits near the upper edge of that cloud together with a subgroup of another dozen stars with rather thick- disk kinematics.

Thus, about two thirds of the MG stars considered here are compatible with thin-disk stars, while the remainder, and markedly Hip 22336, is found at a higher deviation from the circular $V_{\rm LSR}$-component (i.e., high T), and is located toward thick-disk stars. We thus ascertain a dynamical admixture of the thick disk during the resonant formation of this MG, as also indicated by the advanced age of those stars. Additionally,

[4] Here, `CylSpline` refers to AGAMA's cylindrical-spline representation of the potential, in which the radial and vertical dependence is tabulated on a cylindrical grid and the azimuthal structure is represented by Fourier harmonics.

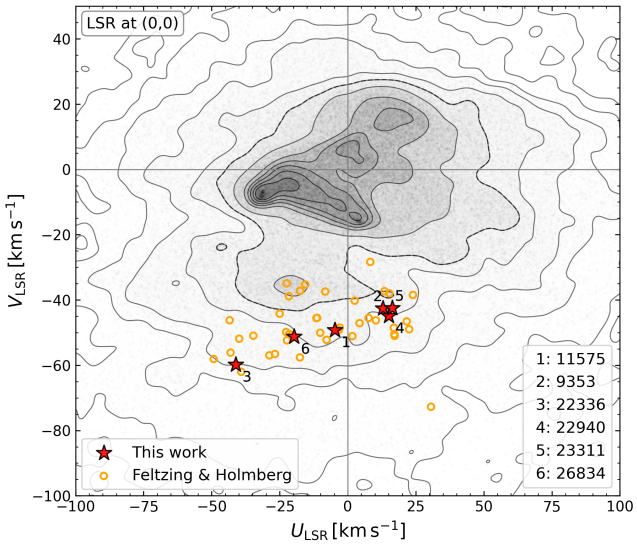


Fig. 10. Velocity distribution in the solar neighborhood showing the GALAH field-star density (gray shading) with kernel–density contours (black) in the (U_{LSR}, V_{LSR}) plane. Red stars mark our MG members; open orange circles show the comparison sample from Feltzing & Holmberg (2000). The crosshair indicates the Local Standard of Rest (LSR) at (0, 0). Numbers next to the red symbols correspond to the Hip-identifiers listed in the legend.

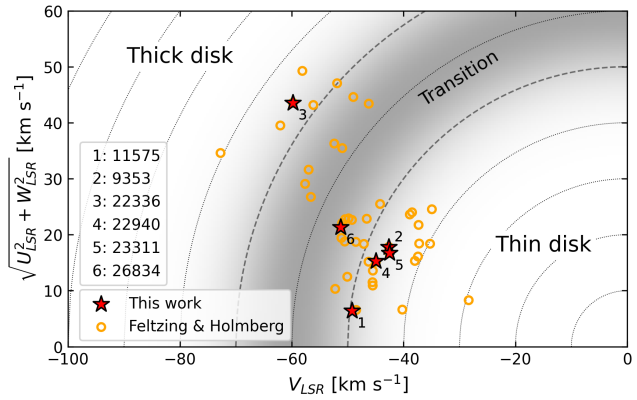


Fig. 11. Toomre diagram for HR 1614 MG members. Red stars mark stars analyzed in this work (numbers indicate Hip-identifiers); orange open circles show members from Feltzing & Holmberg (2000). Dotted curves trace illustrative loci of constant total space velocity with respect to the LSR. The shaded background with dashed guides only schematically indicates the thin–disk, transition, and thick–disk regimes commonly used in Toomre space (e.g., Bensby et al. 2003).

the elevated Z_{max} and eccentricity of such stars, in particular Hip 22336, are an indicator of a fraction of the HR 1614-group stars coming from the thick disk. However, the star with the strongest thick disk-like chemical evidence is kinematically closer to the thin disk. This is in line with the existence of kinematically thick-disk stars among the chemically thin-disk population, and vice versa. As argued from the chemical analysis above (Sect. 4.3) this makes the star Hip 22336 (with thin-disk abundances and thick-disk dynamics) a common representative of the chemodynamic crucible of this MG (see also McWilliam 2016; their Fig. 2). Finally, we note that the inclusion of the bar in the potential on top of a regular, axisymmetric potential (e.g., McMillan 2017) results in a decrease in the mean galactocentric

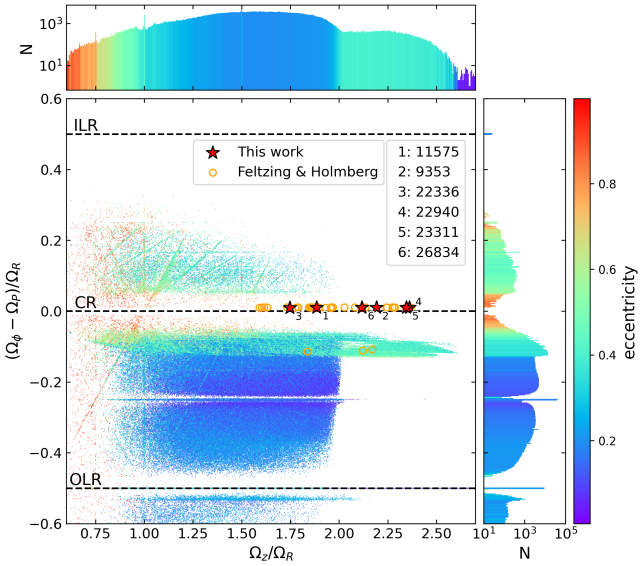


Fig. 12. Frequency-ratio map for the HR 1614 MG relative to a rigidly rotating non–axisymmetric pattern. The main panel shows $(\Omega_\phi - \Omega_p)/\Omega_R$ vs. Ω_z/Ω_R; background points (color–coded by eccentricity) depict a comparison disk sample, with the top and right panels giving the corresponding 1D distributions. Horizontal dashed lines indicate the resonant loci for an $m = 2$ perturbation: corotation (CR; $(\Omega_\phi - \Omega_p)/\Omega_R = 0$), inner Lindblad resonance (ILR; $+1/2$), and outer Lindblad resonance (OLR; $-1/2$). Red symbols mark the six stars analyzed in this work (numbers label *Hipparcos* IDs); orange open circles show literature candidates from Feltzing & Holmberg (2000). The three orange points below the CR line at $y \simeq -0.09$ form a higher-angular-momentum tail of the literature comparison sample.

radii of the stars (as detailed in Appendix B and Table B.2), highlighting the importance of the bar for inducing significant orbital changes.

6.3. Orbital resonances

Figure 12 shows a frequency map for our MG stars against a large comparison sample of ∼4.6×10^5 disk stars from *GALAH* DR4 (Buder et al. 2025). We computed the three fundamental orbital frequencies Ω_R, Ω_ϕ, and Ω_z, which characterize the radial epicycle, the mean azimuthal rotation, and the vertical oscillation of an orbit (e.g. Binney & Tremaine 2008). In the inertial frame, our adopted MW mass model is time dependent, whereas in the frame corotating with the bar at constant pattern speed Ω_p it is time independent (i.e., steady). In either case, resonant lines appear as straight loci in the $(\Omega_z/\Omega_R,\ (\Omega_\phi - \Omega_p)/\Omega_R)$ plane (Valluri et al. 2010, 2016; Bovy 2026). Frequencies were measured from the integrated phase–space time series with the `naif` Python package, which implements the numerical analysis of fundamental frequencies (NAFF) algorithm (Laskar 1993; Valluri & Merritt 1998; Beraldo e Silva et al. 2023). This spectral approach robustly recovers the dominant quasiperiodic components and is well suited to highlight bar resonances as straight loci in the frequency–ratio space (Monari et al. 2019).

We integrated the orbits into our adopted MW potential and determined the inertial-frame frequencies $(\Omega_\phi, \Omega_R, \Omega_z)_{\rm ini}$. For a rotating bar with pattern speed Ω_p, we transformed these to the bar-frame by subtracting the pattern rotation from the azimuthal angle and the corresponding velocity field, which then allowed us to re-measure the bar-frame frequencies $(\Omega_\phi, \Omega_R, \Omega_z)_{\rm bar}$. As a consistency check we verified that $\Omega_{\phi,\rm ini} - \Omega_p \simeq \Omega_{\phi,\rm bar}$ is

within numerical tolerance. In Fig. 12, we show dimensionless ratios $x \equiv \Omega_z/\Omega_R$ and $y \equiv (\Omega_\phi - \Omega_p)/\Omega_R$, which compactly encode in–plane and vertical frequency information (Binney & Tremaine 2008; Monari et al. 2019). For the six stars analyzed in this work, the plotted quantities are based on the same Monte Carlo realizations used for the orbital parameters.

In a rotating non-axisymmetric potential the general resonance condition is $m(\Omega_\phi - \Omega_p) = \ell\,\Omega_R + n\,\Omega_z$, with integers (m, ℓ, n). For a bisymmetric bar ($m = 2$), ($n = 0$), in–plane resonances appear at corotation ($y = 0$) and as the ILR and OLR, respectively ($y = \pm\frac{1}{2}$). Vertical families ($n \neq 0$), in turn, map to straight lines $y = (n/m)\,x - \ell/m$ and generate the fan of thin slanted ridges in the background distribution of Fig. 12, where the vertical oscillation frequency is commensurable with the combination of radial and azimuthal motion. In our fully 3D non-axisymmetric MW potential several low-order (ℓ, n) families overlap in frequency space, so individual ridges are blends rather than pure resonances; therefore, we only refer to them generically as vertical ($n \neq 0$) families.

The concentration of points along the CR line and the clarity of the ILR and/or OLR bands are a direct consequence of using a dynamically consistent potential and a pattern speed matched to it: with a mismatched Ω_p, the same stars would shear vertically (changing y) and the resonant ridges would blur (Dehnen 2000; Monari et al. 2019). That the resonant structure emerges cleanly is therefore a useful validation of our choice of both the potential and frequency-extraction methods.

For context, in Fig. 12 we overplot a set of literature comparisons drawn from *GALAH* DR4 (Buder et al. 2025) following the best-practice recommendations of DR4 with S/N > 30 and supplemented by conservative cuts (`vsini`< 15 km s^{-1}, `e_rv_comp_1`< 1 km s^{-1}). Our six MG stars and all but three of the literature stars from Feltzing & Holmberg (2000) occupy a compact region in frequency space. They span approximately $1.75 \lesssim \Omega_z/\Omega_R \lesssim 2.36$ and lie very close to the CR line, with $(\Omega_\phi - \Omega_p)/\Omega_R \simeq 0$. We therefore interpret them as stars on the CR rather than as members of other, distinct resonant families. The spread in Ω_z/Ω_R reflects the different vertical orbital structures of the stars, consistent with the small but measurable differences in $Z_{\rm max}$ and eccentricity discussed above. We also note that the small values of the stars' frequency drift[5], $\log \Delta\Omega$ at CR (see also Table B.1), which indicates no significant chaotic behavior in their orbits.

In contrast, three Feltzing & Holmberg (2000) candidates below the CR line are offset to $y \simeq -0.09$. In the same calculation they have larger absolute angular momenta, $|L_z| \simeq 1.60$–1.66×10^3 kpc km s^{-1}, and larger present-day azimuthal velocities, $|V_\phi| \simeq 197$–204 km s^{-1}, than the remainder of the sample. We regard them as a higher-angular-momentum extension of the original literature selection rather than as part of the very compact CR clump traced by our sample. Finally, we note that the CR coordinate y above changes by less than 10^{-4} upon including the spiral-arm potential, so our identification of the CR resonance remains unaffected.

The broad distribution of disk stars outlines well-known resonant ridges associated with the Galactic bar. Similar structures have been linked to the Hercules stream and other local MGs in both models and data (Dehnen & Binney 1998; Dehnen 2000; Monari et al. 2017, 2019). The alignment of our stars with the CR ridge then supports the interpretation that they belong to a resonantly influenced disk population.

[5] $\Delta\Omega = \max_{i=1,2,3} \left| \frac{\Omega_i(T_2) - \Omega_i(T_1)}{\Omega_i(T_1)} \right|$, where the three frequencies are evaluated in two separate parts (T_1, T_2) over the orbits (Valluri et al. 2010).

7. Discussion and conclusions

Even though the entire HR 1614 MG contains a large number of $O(10^4)$ candidates (Kushniruk et al. 2020), the six members studied here at high resolution and in great chemical detail offer a valuable insight into the origin of those stars. In particular, by accounting for a realistic potential of the rotating bar and from the ensuing frequency analysis, we established that the stars' common motion originated from a CR resonance with the MW bar. Overall, our results are in very good agreement with the chemical abundance study of De Silva et al. (2007). Notably, Hip 23311 is chemically in line with a thick disk heritage, while Hip 22336, and possibly Hip 26834, are more closely kinematic members of the thick disk than the thin disk.

Numerous mechanisms can perturb any preexisting population such as the MW disk(s). For instance, Minchev et al. (2009) investigated a merging dwarf galaxy, which can induce stream-like perturbations in the form of a "ringing" disk. The ensuing phase-space waves by such mergers rather constitute dispersed star formation events that would lead to chemical element spreads, leaving a chemical signature dissimilar from disrupted clusters (e.g., Kushniruk & Bensby 2019). Crossings through the transient spiral arms also play a role in the formation of stream-like structures (Quillen et al. 2018a,b), although this interpretation is ruled out by the older HR 1614 MG.

The Galactic bar is responsible for the formation of many coherent dynamical features observed (e.g., Dehnen 2000; Trick et al. 2021; Wheeler et al. 2022). In particular, the bar is able to trap stars of any ages, so that any dynamical influence is not restricted to stars younger than the bar. Li et al. (2025a,b) performed a chemodynamic study from archival APOGEE and GALAH data from the Hercules stream, of which the HR 1614 MG is a purported subgroup, adding further insight into the complex effects of resonant disk-stirring.

The six stars studied here can only graze the surface of understanding the origin of the large dynamical groups. It is therefore imperative to also exploit ongoing or upcoming large spectroscopic surveys to sample their grand abundance space, such as offered by the 4MOST, MOONS, WEAVE, or SDSS-V Skymapper campaigns (Cirasuolo et al. 2011; de Jong et al. 2012; Kollmeier et al. 2017; Bensby et al. 2019; Gonzalez et al. 2020).

Data availability

The full Table 1 is available at the CDS via `https://cdsarc.cds.unistra.fr/viz-bin/cat/J/A+A/714/A14`.

Acknowledgements. We are grateful to J. Bovy, E. Caffau, W. Dehnen, and S. Reffert for helpful discussions. This research made use of atomic data from the INSPECT database (`https://www.inspect-stars.com`).

References

Amarsi, A. M., Nissen, P. E., & Skúladóttir, Á. 2019, A&A, 630, A104
Amarsi, A. M., Li, W., Grevesse, N., & Jurewicz, A. J. G. 2025, A&A, 703, A35
Anderson, S. R., Gough-Kelly, S., Debattista, V. P., et al. 2024, MNRAS, 527, 2919
Antipova, L. I., & Boyarchuk, A. A. 2016, Astron. Rep., 60, 145
Antoja, T., Figueras, F., Fernández, D., & Torra, J. 2008, A&A, 490, 135
Asplund, M., Grevesse, N., Sauval, A. J., & Scott, P. 2009, ARA&A, 47, 481
Bailer-Jones, C. A. L., Rybizki, J., Fouesneau, M., Mantelet, G., & Andrae, R. 2018, AJ, 156, 58

Battistini, C., & Bensby, T. 2015, A&A, 577, A9
Bensby, T., Feltzing, S., & Lundström, I. 2003, A&A, 410, 527
Bensby, T., Bergemann, M., Rybizki, J., et al. 2019, Messenger, 175, 35
Bensby, T., Feltzing, S., & Oey, M. S. 2014, A&A, 562, A71
Beraldo e Silva, L., Debattista, V. P., Anderson, S. R., et al. 2023, ApJ, 955, 38
Bergemann, M. 2011, MNRAS, 413, 2184
Bergemann, M., & Gehren, T. 2008, A&A, 492, 823
Bergemann, M., & Cescutti, G. 2010, A&A, 522, A9
Bergemann, M., Pickering, J. C., & Gehren, T. 2010, MNRAS, 401, 1334
Bergemann, M., Kudritzki, R.-P., Würl, M., et al. 2013, ApJ, 764, 115
Bergemann, M., Collet, R., Amarsi, A. M., et al. 2017, ApJ, 847, 15
Binney, J., & Tremaine, S. 2008, Galactic Dynamics, 2nd edn. (Princeton University Press)
Blitz, L., & Spergel, D. N. 1991, ApJ, 379, 631
Bovy, J. 2026, Dynamics and Astrophysics of Galaxies (Princeton, NJ: Princeton University Press; in press)
Buder, S., Kos, J., Wang, X. E., et al. 2025, PASA, 42, e051
Busso, M., Gallino, R., & Wasserburg, G. J. 1999, ARA&A, 37, 239
Caffau, E., Bonifacio, P., Faraggiana, R., et al. 2005, A&A, 441, 533
Caliskan, S., Amarsi, A. M., Racca, M., et al. 2025, A&A, 696, A210
Carollo, D., Beers, T. C., Lee, Y. S., et al. 2007, Nature, 450, 1020
Casali, G., Spina, L., Magrini, L., et al. 2020, A&A, 639, A127
Castelli, F., & Kurucz, R. L. 2003, in IAU Symposium, 210, Modelling of Stellar Atmospheres, eds. N. Piskunov, W. W. Weiss, & D. F. Gray, A20
Chiba, R., Friske, J. K. S., & Schönrich, R. 2021, MNRAS, 500, 4710
Cirasuolo, M., Afonso, J., Bender, R., et al. 2011, Messenger, 145, 11
de Jong, R. S., Bellido-Tirado, O., Chiappini, C., et al. 2012, Proc. SPIE, 8446, 84460T
De Silva, G. M., Freeman, K. C., Bland-Hawthorn, J., Asplund, M., & Bessell, M. S. 2007, AJ, 133, 694
Debattista, V. P., Gonzalez, O. A., Sanderson, R. E., et al. 2019, MNRAS, 485, 5073
Dehnen, W. 2000, AJ, 119, 800
Dehnen, W., & Binney, J. 1998, MNRAS, 294, 429
Delgado Mena, E., Tsantaki, M., Adibekyan, V. Z., et al. 2017, A&A, 606, A94
Den Hartog, E. A., Lawler, J. E., Sobeck, J. S., Sneden, C., & Cowan, J. J. 2011, ApJS, 194, 35
D'Onghia, E., & L. Aguerri, J. A. 2020, ApJ, 890, 117
Dotter, A., Chaboyer, B., Jevremović, D., et al. 2008, ApJS, 178, 89
Eggen, O. J. 1958, MNRAS, 118, 65
Eggen, O. J. 1965, in Galactic Structure, eds. A. Blaauw, & M. Schmidt (University of Chicago Press), 111
Eggen, O. J. 1971, ApJS, 22, 389
Eggen, O. J. 1977, PASP, 89, 706
Eggen, O. J. 1978, ApJ, 222, 203
Eggen, O. J. 1992, AJ, 104, 1906
Feltzing, S., & Holmberg, J. 2000, A&A, 357, 153
Franchini, M., Morossi, C., Di Marcantonio, P., et al. 2021, AJ, 161, 9
Frankel, N., Sanders, J., Ting, Y.-S., & Rix, H.-W. 2020, ApJ, 896, 15
Fulbright, J. P., McWilliam, A., & Rich, R. M. 2006, ApJ, 636, 821
Gagné, J., Faherty, J. K., Moranta, L., & Popinchalk, M. 2021, ApJ, 915, L29
Gaia Collaboration (Vallenari, A., et al.) 2023, A&A, 674, A1
Gallagher, A. J., Bergemann, M., Collet, R., et al. 2020, A&A, 634, A55
Gilmore, G., & Reid, N. 1983, MNRAS, 202, 1025
Gonzalez, O. A., Mucciarelli, A., Origlia, L., et al. 2020, Messenger, 180, 18
Gran, F., Zoccali, M., Rojas-Arriagada, A., et al. 2021, MNRAS, 504, 3494
Green, G. M., Schlafly, E., Zucker, C., Speagle, J. S., & Finkbeiner, D. 2019, ApJ, 887, 93
Haywood, M. 2008, MNRAS, 388, 1175
Hufnagel, B., & Smith, G. H. 1994, PASP, 106, 1068
Hunt, J. A. S., & Bovy, J. 2018, MNRAS, 477, 3945
Hunter, G. H., Sormani, M. C., Beckmann, J. P., et al. 2024, A&A, 692, A216
Johnson, J. A., Ivans, I. I., & Stetson, P. B. 2006, ApJ, 640, 801
Keller, S. C., Schmidt, B. P., Bessell, M. S., et al. 2007, PASA, 24, 1
Kelson, D. D. 2003, PASP, 115, 688
Kelson, D. D., Illingworth, G. D., van Dokkum, P. G., & Franx, M. 2000, ApJ, 531, 159
Kobayashi, C., Karakas, A. I., & Lugaro, M. 2020, ApJ, 900, 179
Koch, A., & Caffau, E. 2011, A&A, 534, A52
Koch, A., & Edvardsson, B. 2002, A&A, 381, 500
Koch, A., & McWilliam, A. 2008, AJ, 135, 1551
Koch, A., & McWilliam, A. 2014, A&A, 565, A23
Koch, A., Rich, R. M., Reitzel, D. B., et al. 2008, ApJ, 689, 958
Koch, A., Hansen, T. T., & Kunder, A. 2018, A&A, 609, A13
Koch-Hansen, A. J., Hansen, C. J., & McWilliam, A. 2021, A&A, 653, A2
Kollmeier, J. A., Zasowski, G., Rix, H.-W., et al. 2017, arXiv e-prints [arXiv:1711.03234]
Kordopatis, G., Gilmore, G., Wyse, R. F. G., et al. 2013, MNRAS, 436, 3231
Kunder, A., Pérez-Villegas, A., Rich, R. M., et al. 2020, AJ, 159, 270
Kushniruk, I., & Bensby, T. 2019, A&A, 631, A47
Kushniruk, I., Bensby, T., Feltzing, S., et al. 2020, A&A, 638, A154
Laskar, J. 1993, Celest. Mech. Dyn. Astron., 56, 191
Lawler, J. E., Sneden, C., & Cowan, J. J. 2015, ApJS, 220, 13
Lawler, J. E., Hala, Sneden, C., et al. 2019, ApJS, 241, 21
Leung, H. W. 2024, mw_plot: Milky Way plotting package, https://milkyway-plot.readthedocs.io/en/stable/, accessed 2025-11-11
Li, Y., Freeman, K., & Jerjen, H. 2025a, MNRAS, 539, 1595
Li, Y., Freeman, K., Jerjen, H., et al. 2025b, MNRAS, 538, 1963
Lind, K., Asplund, M., Barklem, P. S., & Belyaev, A. K. 2011, A&A, 528, A103
Mashonkina, L., & Christlieb, N. 2014, A&A, 565, A123
Mashonkina, L., Korn, A. J., & Przybilla, N. 2007, A&A, 461, 261
McMillan, P. J. 2017, MNRAS, 465, 76
McWilliam, A. 2016, PASA, 33, e040
McWilliam, A., & Smecker-Hane, T. A. 2005, ApJ, 622, L29
McWilliam, A., & Zoccali, M. 2010, ApJ, 724, 1491
McWilliam, A., Preston, G. W., Sneden, C., & Searle, L. 1995, AJ, 109, 2757
McWilliam, A., Rich, R. M., & Smecker-Hane, T. A. 2003, ApJ, 592, L21
Minchev, I., Quillen, A. C., Williams, M., et al. 2009, MNRAS, 396, L56
Mishenina, T. V., Gorbaneva, T. I., Basak, N. Y., Soubiran, C., & Kovtyukh, V. V. 2011, Astron. Rep., 55, 689
Mishenina, T., Pignatari, M., Carraro, G., et al. 2015, MNRAS, 446, 3651
Monari, G., Kawata, D., Hunt, J. A. S., & Famaey, B. 2017, MNRAS, 466, L113
Monari, G., Famaey, B., Siebert, A., Wegg, C., & Gerhard, O. 2019, A&A, 626, A41
Nepal, S., Chiappini, C., Guiglion, G., et al. 2024, A&A, 681, L8
Ness, M. K., Wheeler, A. J., McKinnon, K., et al. 2022, ApJ, 926, 144
Nguyen, C. T., Costa, G., Girardi, L., et al. 2022, A&A, 665, A126
Nissen, P. E., Amarsi, A. M., Skúladóttir, Á., & Schuster, W. J. 2024, A&A, 682, A116
Nordlander, T., & Lind, K. 2017, A&A, 607, A75
Paunzen, E. 2022, A&A, 661, A89
Piatti, A. E., & Koch, A. 2018, ApJ, 867, 8
Prochaska, J. X., Naumov, S. O., Carney, B. W., McWilliam, A., & Wolfe, A. M. 2000, AJ, 120, 2513
Queiroz, A. B. A., Anders, F., Santiago, B. X., et al. 2018, MNRAS, 476, 2556
Quillen, A. C., Carrillo, I., Anders, F., et al. 2018a, MNRAS, 480, 3132
Quillen, A. C., De Silva, G., Sharma, S., et al. 2018b, MNRAS, 478, 228
Ramírez, I. & Meléndez, J. 2005, ApJ, 626, 465
Ramos, P., Antoja, T., & Figueras, F. 2018, A&A, 619, A72
Reggiani, H., Amarsi, A. M., Lind, K., et al. 2019, A&A, 627, A177
Ruchti, G. R., Bergemann, M., Serenelli, A., Casagrande, L., & Lind, K. 2013, MNRAS, 429, 126
Sanders, J. L., Kawata, D., Matsunaga, N., et al. 2024, MNRAS, 530, 2972
Schlafly, E. F., & Finkbeiner, D. P. 2011, ApJ, 737, 103
Sellwood, J. A., & Binney, J. J. 2002, MNRAS, 336, 785
Shi, J. R., Yan, H. L., Zhou, Z. M., & Zhao, G. 2018, ApJ, 862, 71
Sinha, A., Zasowski, G., Frinchaboy, P., et al. 2024, ApJ, 975, 89
Sitnova, T. M., Mashonkina, L. I., & Ryabchikova, T. A. 2013, Astron. Lett., 39, 126
Smith, G. H. 1983, AJ, 88, 1775
Sneden, C. A. 1973, PhD thesis, The University of Texas at Austin.
Stanek, K. Z., Udalski, A., Szymański, M., et al. 1997, ApJ, 477, 163
Steffen, M., Prakapavičius, D., Caffau, E., et al. 2015, A&A, 583, A57
Takeda, Y., Zhao, G., Chen, Y.-Q., Qiu, H.-M., & Takada-Hidai, M. 2002, PASJ, 54, 275
Tautvaišienė, G., Viscasillas Vázquez, C., Mikolaitis, Š., et al. 2021, A&A, 649, A126
Tonry, J., & Davis, M. 1979, AJ, 84, 1511
Trick, W. H., Fragkoudi, F., Hunt, J. A. S., Mackereth, J. T., & White, S. D. M. 2021, MNRAS, 500, 2645
Valluri, M., & Merritt, D. 1998, ApJ, 506, 686
Valluri, M., Debattista, V. P., Quinn, T., & Moore, B. 2010, MNRAS, 403, 525
Valluri, M., Shen, J., Abbott, C., & Debattista, V. P. 2016, ApJ, 818, 141
Vasiliev, E. 2019, MNRAS, 482, 1525
Venn, K. A., Irwin, M., Shetrone, M. D., et al. 2004, AJ, 128, 1177
Walker, M. G., Mateo, M., Olszewski, E. W., et al. 2006, AJ, 131, 2114
Wegg, C., & Gerhard, O. 2013, MNRAS, 435, 1874
Wheeler, A., Abril-Cabezas, I., Trick, W. H., Fragkoudi, F., & Ness, M. 2022, ApJ, 935, 28
Woosley, S. E., & Weaver, T. A. 1995, ApJS, 101, 181
Yang, Y., Zhao, J.-K., Tang, X.-Z., Ye, X.-H., & Zhao, G. 2023, ApJ, 953, 130
Zhao, G., Mashonkina, L., Yan, H. L., et al. 2016, ApJ, 833, 225

Appendix A: Abundance errors and results

Table A.1. Systematic errors, exemplary for star Hip 11575.

Species	T_{eff} ± 100 K	log g ± 0.10 dex	[Fe/H] ± 0.10 dex	v_{mic} ± 0.10 km s^{-1}	AODFNEW	σ_{Tot}
C I	∓0.08	±0.04	<0.01	<0.01	+0.05	0.09
O I	∓0.11	±0.03	±0.01	∓0.01	+0.10	0.11
Na I	±0.05	∓0.02	<0.01	∓0.01	+0.02	0.05
Mg I	±0.04	∓0.01	<0.01	∓0.01	<0.01	0.04
Al I	±0.04	<0.01	<0.01	∓0.01	−0.01	0.04
Si I	±0.02	<0.01	<0.01	∓0.01	+0.02	0.03
K I	±0.08	∓0.04	±0.01	∓0.03	+0.04	0.09
Ca I	±0.06	∓0.02	<0.01	∓0.03	+0.01	0.07
Sc II	∓0.01	±0.04	±0.02	∓0.03	+0.11	0.06
Ti I	±0.09	<0.01	<0.01	∓0.01	−0.02	0.09
Ti II	∓0.01	±0.04	±0.02	∓0.05	+0.10	0.07
V I	±0.10	<0.01	<0.01	∓0.01	−0.02	0.10
Cr I	±0.08	∓0.01	<0.01	∓0.03	−0.01	0.08
Mn I	±0.09	∓0.01	∓0.01	∓0.06	<0.01	0.11
Fe I	±0.07	∓0.01	<0.01	∓0.04	+0.01	0.08
Fe II	∓0.03	±0.04	±0.02	∓0.04	+0.11	0.08
Co I	±0.08	<0.01	<0.01	∓0.01	−0.01	0.08
Ni I	±0.07	<0.01	<0.01	∓0.03	+0.01	0.07
Cu I	±0.10	∓0.01	<0.01	∓0.06	+0.01	0.11
Y II	<0.01	±0.04	±0.03	∓0.03	+0.10	0.06
Zr II	<0.01	±0.04	±0.03	∓0.01	+0.09	0.06
Ba II	±0.03	±0.02	±0.04	∓0.07	+0.14	0.09
La II	±0.02	±0.04	±0.03	<0.01	+0.10	0.06
Ce II	±0.01	±0.04	±0.03	∓0.01	+0.09	0.06
Nd II	±0.01	±0.04	±0.03	∓0.04	+0.10	0.07
Eu II	<0.01	±0.04	±0.03	∓0.01	+0.10	0.06

Table A.2. LTE abundance results. Abundance ratios for ionized species are given relative to Fe II. For iron itself, [Fe/H] is listed. The line-to-line scatter, σ, and number of measured lines, N, indicate the statistical error.

Species	Hip 11575			Hip 9353			Hip 22336			Hip 22940		
	[X/Fe]	σ	N	[X/Fe]	σ	N	[X/Fe]	σ	N	[X/Fe]	σ	N
C I	−0.04	0.12	2	−0.20	0.03	2	−0.19	0.06	2	0.02	0.09	2
O I	0.10	0.02	3	0.06	0.05	3	0.02	0.02	3	0.06	0.03	3
Na I	0.19	0.06	4	0.25	0.12	4	0.02	0.10	4	0.14	0.17	4
Mg I	0.04	0.14	4	0.01	0.06	3	−0.03	0.03	4	−0.05	0.12	4
Al I	0.03	0.03	3	0.04	0.08	3	−0.05	0.05	3	0.12	0.02	3
Si I	−0.02	0.13	13	−0.00	0.15	13	−0.04	0.11	13	0.01	0.10	13
S I	−0.06	0.07	5	−0.15	0.07	5	−0.20	0.14	5	−0.08	0.06	5
K I	0.44	…	1	0.46	…	1	0.33	…	1	0.13	…	1
Ca I	−0.01	0.09	15	0.02	0.16	15	0.00	0.13	15	0.01	0.12	14
Sc I	−0.05	0.10	4	0.06	0.18	5	0.07	0.16	5	0.19	0.10	6
Ti I	−0.08	0.11	23	0.02	0.16	22	0.00	0.12	23	0.15	0.16	23
Ti II	0.09	0.10	4	0.09	0.19	6	0.23	0.17	4	0.26	0.21	5
V I	−0.06	0.02	4	0.01	0.09	4	−0.10	0.06	4	0.14	0.20	4
Cr I	−0.05	0.23	9	0.07	0.13	7	−0.01	0.17	8	0.02	0.06	8
Mn I	−0.08	0.09	6	−0.06	0.07	6	−0.17	0.10	6	0.02	0.17	4
Fe I	0.20	0.12	111	0.32	0.10	112	0.30	0.12	113	0.17	0.13	102
Fe II	0.20	0.11	16	0.31	0.12	16	0.30	0.11	15	0.17	0.10	14
Co I	0.06	0.14	11	0.06	0.19	11	−0.07	0.12	11	0.14	0.31	11
Ni I	0.02	0.18	26	−0.01	0.12	26	−0.03	0.11	26	0.08	0.16	25
Cu I	0.05	0.10	3	0.17	0.10	3	−0.11	0.09	3	0.07	0.23	3
Y II	−0.12	0.23	3	−0.16	0.10	3	−0.18	0.02	3	−0.04	0.17	3
Zr II	−0.12	…	1	−0.35	…	1	−0.31	…	1	−0.14	…	1
Ba II	−0.19	0.04	3	−0.07	0.08	3	−0.03	0.06	3	0.08	0.13	3
La II	−0.02	0.01	2	0.13	0.04	2	0.20	0.01	2	0.37	0.18	2
Ce II	−0.01	…	1	−0.20	…	1	0.02	…	1	0.24	…	1
Eu II	0.10	…	1	−0.10	…	1	−0.32	…	1	0.01	…	1
$[hs/ls]^a$	0.27	…	…	0.82	…	…	0.99	…	…	0.86	…	…

Species	Hip 23311			Hip 26834			Intrinscic Scatter
	[X/Fe]	σ	N	[X/Fe]	σ	N	σ_0
C I	0.28	0.09	2	−0.18	0.05	2	0.25±0.07
O I	0.20	0.16	3	−0.08	0.05	3	0.06±0.02
Na I	0.39	0.23	4	0.15	0.13	4	0.07±0.04
Mg I	0.18	0.06	4	0.24	0.36	5	0.08±0.03
Al I	0.19	0.16	3	0.11	0.05	3	0.07±0.03
Si I	0.15	0.14	13	−0.03	0.12	13	0.05±0.02
S I	−0.24	0.25	3	−0.13	0.04	4	0.02±0.02
K I	0.17	…	1	0.16	…	1	0.14±0.04
Ca I	0.09	0.06	4	−0.01	0.14	13	0.02±0.02
Sc I	0.10	0.20	5	0.10	0.12	5	0.06±0.03
Ti I	0.30	0.13	22	0.04	0.11	22	0.12±0.04
Ti II	0.11	0.13	6	0.27	0.17	4	0.32±0.16
V I	0.32	0.17	4	0.02	0.15	4	0.12±0.05
Cr I	0.07	0.07	7	0.00	0.15	8	0.17±0.09
Mn I	0.10	0.17	6	−0.03	0.15	6	0.05±0.03
Fe I	0.13	0.17	115	0.38	0.13	108	0.09±0.03
Fe II	0.14	0.15	13	0.38	0.16	16	0.08±0.03
Co I	0.18	0.17	10	0.01	0.16	9	0.07±0.03
Ni I	0.06	0.20	25	0.06	0.15	27	0.03±0.02
Cu I	0.11	0.23	2	0.04	0.18	3	0.08±0.04
Y II	0.41	…	1	−0.09	0.16	3	0.21±0.06
Zr II	0.39	…	1	−0.31	…	1	0.25±0.07
Ba II	0.18	0.19	3	0.04	0.09	3	0.08±0.03
La II	0.25	…	1	0.32	0.07	2	0.12±0.04
Ce II	0.24	…	1	0.01	…	1	0.16±0.04
Eu II	−0.01	…	1	0.05	…	1	0.14±0.04
$[hs/ls]^a$	−0.40	…	…	0.97	…	…	

Notes. [a] $[hs/ls]$ = [<Ba,La>/<Y,Zr>]

Table B.1. Observed and derived kinematic properties.

Parameter	Hip 11575	Hip 9353	Hip 22336	Hip 22940	Hip 23311	Hip 26834
Distance [pc]	98.18 ± 0.14	31.75 ± 0.06	26.12 ± 0.02	36.03 ± 0.03	8.84 ± 0.002	30.06 ± 0.02
μ_α [mas yr^{-1}]	99.81 ± 0.01	230.83 ± 0.14	311.41 ± 0.04	151.02 ± 0.03	549.31 ± 0.02	243.76 ± 0.02
μ_δ [mas yr^{-1}]	−53.79 ± 0.06	−256.47 ± 0.05	−248.83 ± 0.04	−292.11 ± 0.02	−1108.25 ± 0.02	−117.81 ± 0.02
v_{HC} [km s^{-1}]	37.17 ± 0.12	−18.50 ± 0.14	77.12 ± 0.12	14.96 ± 0.12	21.36 ± 0.12	59.16 ± 0.12
X [pc]	−9.9	−16.2	−20.8	−31.7	−7.1	−21.4
Y [pc]	−40.1	7.8	−9.0	−9.1	−3.3	−17.8
Z [pc]	−89.1	−26.2	−13.0	−14.6	−4.0	−11.4
U_{LSR} [km s^{-1}]	-4.78 ± 1.26	12.86 ± 1.25	-41.19 ± 1.25	15.05 ± 1.25	16.35 ± 1.25	-19.72 ± 1.25
V_{LSR} [km s^{-1}]	-49.25 ± 2.06	-42.64 ± 2.06	-59.81 ± 2.06	-44.93 ± 2.06	-42.54 ± 2.06	-51.26 ± 2.06
W_{LSR} [km s^{-1}]	-4.24 ± 0.64	12.29 ± 0.64	-14.19 ± 0.63	-2.52 ± 0.63	-3.50 ± 0.63	8.18 ± 0.62
E [km^2 s^{-2}]	-183738^{+11}_{-11}	-184402^{+12}_{-12}	-181499^{+10}_{-10}	-184178^{+9}_{-9}	-184421^{+4}_{-4}	-183320^{+12}_{-12}
E_J [km^2 s^{-2}]	$-1.837^{+<10^{-3}}_{-<10^{-3}}$	$-1.844^{+<10^{-3}}_{-<10^{-3}}$	$-1.815^{+<10^{-3}}_{-<10^{-3}}$	$-1.842^{+<10^{-3}}_{-<10^{-3}}$	$-1.844^{+<10^{-3}}_{-<10^{-3}}$	$-1.833^{+<10^{-3}}_{-<10^{-3}}$
L_Z [kpc km s^{-1}]	$1491.8^{+0.7}_{-0.7}$	$1546.9^{+0.9}_{-0.9}$	$1408.4^{+0.4}_{-0.4}$	$1530.9^{+0.7}_{-0.7}$	$1545.9^{+0.4}_{-0.4}$	$1478.4^{+0.7}_{-0.7}$
V_R [km s^{-1}]	$3.93^{+0.03}_{-0.03}$	$-12.69^{+0.10}_{-0.10}$	$41.09^{+0.09}_{-0.09}$	$-15.21^{+0.12}_{-0.12}$	$-16.32^{+0.11}_{-0.11}$	$19.28^{+0.11}_{-0.11}$
V_T [km s^{-1}]	$183.44^{+0.09}_{-0.09}$	$190.07^{+0.11}_{-0.11}$	$172.96^{+0.04}_{-0.04}$	$187.75^{+0.09}_{-0.09}$	$190.17^{+0.05}_{-0.05}$	$181.55^{+0.08}_{-0.08}$
R_{Apo} [kpc]	$8.43^{+<0.01}_{-<0.01}$	$8.54^{+<0.01}_{-<0.01}$	$8.57^{+<0.01}_{-<0.01}$	$8.60^{+<0.01}_{-<0.01}$	$8.58^{+<0.01}_{-<0.01}$	$8.46^{+<0.01}_{-<0.01}$
R_{Peri} [kpc]	$3.72^{+<0.01}_{-<0.01}$	$3.72^{+<0.01}_{-<0.01}$	$3.37^{+<0.01}_{-<0.01}$	$3.67^{+<0.01}_{-<0.01}$	$3.69^{+<0.01}_{-<0.01}$	$3.66^{+<0.01}_{-<0.01}$
e	$0.39^{+<0.01}_{-<0.01}$	$0.39^{+<0.01}_{-<0.01}$	$0.44^{+<0.01}_{-<0.01}$	$0.40^{+<0.01}_{-<0.01}$	$0.40^{+<0.01}_{-<0.01}$	$0.40^{+<0.01}_{-<0.01}$
Z_{max} [pc]	$91.6^{+0.9}_{-0.9}$	$186.1^{+5.8}_{-5.8}$	$237.9^{+0.5}_{-0.5}$	$36.6^{+0.8}_{-0.8}$	$56.0^{+1.1}_{-1.1}$	$126.1^{+0.4}_{-0.4}$
P_z [Gyr]	$0.063^{+<10^{-3}}_{-<10^{-3}}$	$0.066^{+<10^{-3}}_{-<10^{-3}}$	$0.067^{+<10^{-3}}_{-<10^{-3}}$	$0.061^{+<10^{-3}}_{-<10^{-3}}$	$0.061^{+<10^{-3}}_{-<10^{-3}}$	$0.065^{+<10^{-3}}_{-<10^{-3}}$
$\Omega_{R,ini}$ [Gyr^{-1}]	$49.08^{+<0.01}_{-<0.01}$	$48.84^{+<0.01}_{-<0.01}$	$56.24^{+<0.01}_{-<0.01}$	$48.85^{+<0.01}_{-<0.01}$	$48.83^{+<0.01}_{-<0.01}$	$49.13^{+<0.01}_{-<0.01}$
$\Omega_{\phi,ini}$ [Gyr^{-1}]	$38.35^{+<0.01}_{-<0.01}$	$38.34^{+<0.01}_{-<0.01}$	$38.35^{+<0.01}_{-<0.01}$	$38.34^{+<0.01}_{-<0.01}$	$38.34^{+<0.01}_{-<0.01}$	$38.35^{+<0.01}_{-<0.01}$
$\Omega_{z,ini}$ [Gyr^{-1}]	$92.54^{+0.05}_{-0.05}$	$107.01^{+0.10}_{-0.10}$	$98.17^{+0.09}_{-0.09}$	$115.34^{+0.03}_{-0.03}$	$114.48^{+0.03}_{-0.03}$	$104.02^{+0.02}_{-0.02}$
$\Omega_{R,bar}$ [Gyr^{-1}]	$49.08^{+<0.01}_{-<0.01}$	$48.84^{+<0.01}_{-<0.01}$	$56.24^{+<0.01}_{-<0.01}$	$48.85^{+<0.01}_{-<0.01}$	$48.83^{+<0.01}_{-<0.01}$	$49.13^{+<0.01}_{-<0.01}$
$\Omega_{\phi,bar}$ [Gyr^{-1}]	$-38.36^{+<0.01}_{-<0.01}$	$-38.34^{+<0.01}_{-<0.01}$	$-38.35^{+<0.01}_{-<0.01}$	$-38.34^{+<0.01}_{-<0.01}$	$-38.34^{+<0.01}_{-<0.01}$	$-38.35^{+<0.01}_{-<0.01}$
$\Omega_{z,bar}$ [Gyr^{-1}]	$92.54^{+0.05}_{-0.05}$	$107.01^{+0.10}_{-0.10}$	$98.17^{+0.09}_{-0.09}$	$115.34^{+0.03}_{-0.03}$	$114.48^{+0.03}_{-0.03}$	$104.02^{+0.02}_{-0.02}$
$\Delta\Omega_R$	$0.00^{+<0.01}_{-<0.01}$	$0.00^{+<0.01}_{-<0.01}$	$0.00^{+<0.01}_{-<0.01}$	$0.00^{+<0.01}_{-<0.01}$	$0.00^{+<0.01}_{-<0.01}$	$0.00^{+0.12}_{-0.12}$
$\Delta\Omega_\phi$	$0.00^{+<0.01}_{-<0.01}$	$0.00^{+<0.01}_{-<0.01}$	$0.00^{+<0.01}_{-<0.01}$	$0.00^{+<0.01}_{-<0.01}$	$0.00^{+<0.01}_{-<0.01}$	$0.00^{+<0.01}_{-<0.01}$
$\Delta\Omega_z$	$0.13^{+<0.01}_{-<0.01}$	$0.19^{+<0.01}_{-<0.01}$	$0.01^{+<0.01}_{-<0.01}$	$0.00^{+<0.01}_{-<0.01}$	$0.00^{+<0.01}_{-<0.01}$	$0.15^{+<0.01}_{-<0.01}$
$\log \Delta\Omega$	$-0.89^{+<0.01}_{-<0.01}$	$-0.72^{+0.01}_{-0.01}$	$-2.21^{+0.04}_{-0.04}$	$-2.98^{+<0.01}_{-<0.01}$	$-2.96^{+0.03}_{-0.03}$	$-0.82^{+0.11}_{-0.11}$

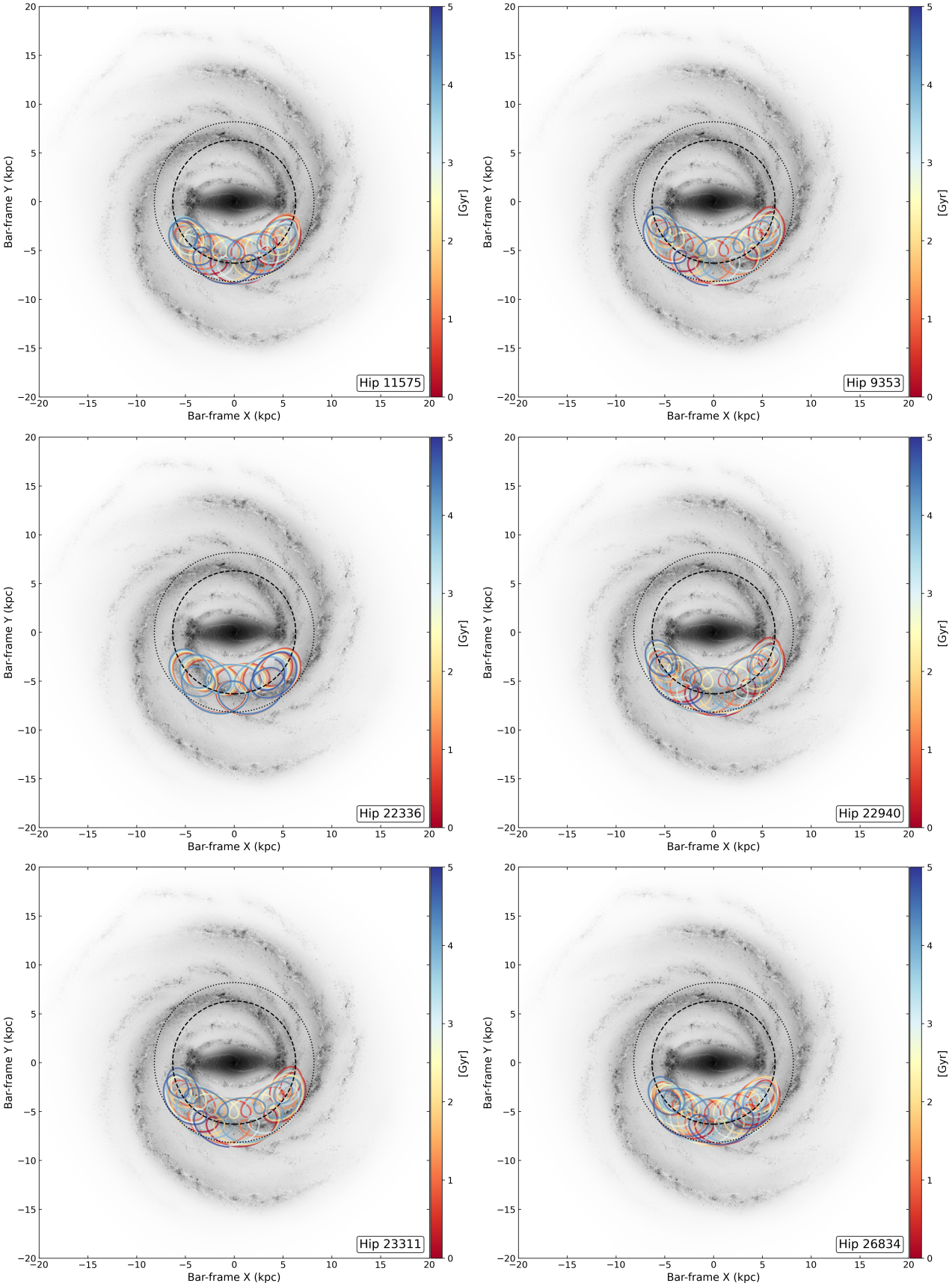


Fig. B.1. Face-on view of the Galactic disk showing the orbits of the six HR 1614 MG stars in the rotating bar frame. The grayscale background shows a schematic MW disk, including the bar and spiral arms, from the `mw-plot` package (Leung 2024). Colored curves trace the stellar orbits over the past 5, Gyr in the potential with a rigidly rotating bar of pattern speed $\Omega_{\rm bar} = 37, {\rm km\,s^{-1}, kpc^{-1}}$. The color encodes the time along each orbit from 0 to 5, Gyr and the dashed line indicates the CR radius at 6.3 kpc, while the dotted circle marks the solar radius at $R_\odot = 8.217\,{\rm kpc}$.

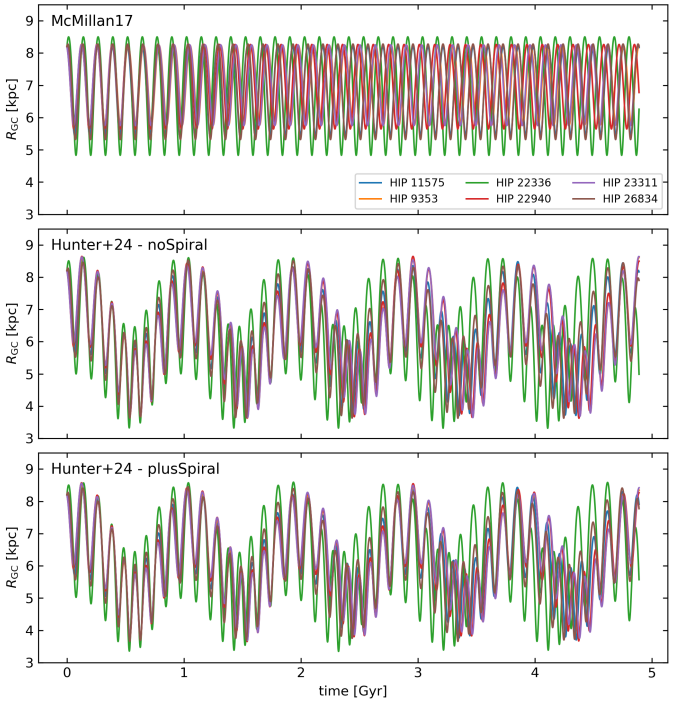


Fig. B.2. Time evolution of the Galactocentric radius, R_{GC}, for the six stars in the axisymmetric potential (top panel), the barred potential without spiral arms (middle panel), and the barred potential including spiral arms (bottom panel).

Appendix B: Time evolution of Galactocentric radii

To quantify the radial extent of the orbits and their dependence on details in the potentials, we illustrate here the time evolution of the Galactocentric radius, R_{GC}, for the six stars in the three different considered Galactic potentials: the axisymmetric potential of McMillan (2017), the nonaxisymmetric potential of Hunter et al. (2024) (labeled "H24" in Table B.2) without spiral arms, and the latter, but including spiral arms. The resulting curves are shown in Fig. B.2, while the corresponding mean, median, minimum, and maximum radii are listed in Table B.2.

In the axisymmetric potential (McMillan 2017), the stars remain on regular radial oscillations around the solar radius. The mean Galactocentric radii lie in a narrow range from 6.88 to 7.10 kpc, with an average over the six stars of $\langle R_{GC} \rangle = 7.00$ kpc. The corresponding median radii are slightly larger, with an average value of 7.13 kpc. The radial excursions are moderate, reaching minimum radii between 4.83 and 5.77 kpc and maximum radii between 8.19 and 8.50 kpc.

The inclusion of the Galactic bar substantially changes the radial behaviour. In the potential of Hunter et al. (2024) without spiral arms, the mean radii decrease to $\langle R_{GC} \rangle = 6.20$ kpc, while the median radii decrease to 6.14 kpc. This corresponds to a reduction of about 0.8 kpc in the mean radius and about 1.0 kpc in the median radius compared to the axisymmetric case. At the same time, the minimum radii become significantly smaller, reaching $R_{GC,min} \simeq 3.3$–3.7 kpc. The maximum radii remain close to, or slightly larger than, those in the axisymmetric model, with values around 8.5–8.6 kpc. Thus, the lower mean and median radii in the barred model are primarily driven by repeated inward radial excursions rather than by a uniform shift of the entire orbit to smaller radii.

Adding spiral arms to the barred potential has only a minor effect on these results. The mean and median radii in the barred model with spiral arms are nearly identical to those obtained without spiral arms, with average values of 6.19 kpc and 6.14 kpc, respectively. For individual stars, the differences in the mean radii between the barred models with and without spiral arms are only at the level of ~0.01 kpc. The time evolution in Fig. B.2 likewise shows that the spiral arms do not qualitatively alter the radial oscillation pattern over the integration time considered here.

Overall, this comparison shows that the non-axisymmetric bar potential has a significant impact on the inferred radial extent of the stellar orbits. Compared to the axisymmetric case, the barred potentials produce smaller mean and median Galactocentric radii and allow the stars to reach substantially smaller pericentric radii. However, the $R_{GC}(t)$ curves remain strongly oscillatory rather than showing a monotonic radial drift.

Table B.2. Mean, median, minimum, and maximum Galactocentric radii for the six stars in the axisymmetric, barred, and barred plus spiral-arm potentials.

Potential	Hip	$\langle R_{GC} \rangle$	$\widetilde{R}_{GC}$	$R_{GC,min}$	$R_{GC,max}$
		[kpc]			
McMillan17	11575	6.938	7.054	5.441	8.193
McMillan17	9353	7.096	7.186	5.772	8.236
McMillan17	22336	6.880	7.080	4.829	8.502
McMillan17	22940	7.066	7.174	5.646	8.266
McMillan17	23311	7.098	7.192	5.750	8.253
McMillan17	26834	6.941	7.077	5.317	8.279
H24 noSpiral	11575	6.196	6.102	3.694	8.480
H24 noSpiral	9353	6.209	6.130	3.665	8.612
H24 noSpiral	22336	6.184	6.244	3.316	8.614
H24 noSpiral	22940	6.218	6.124	3.625	8.644
H24 noSpiral	23311	6.218	6.134	3.647	8.641
H24 noSpiral	26834	6.196	6.115	3.626	8.528
H24 plusSpiral	11575	6.184	6.089	3.700	8.431
H24 plusSpiral	9353	6.195	6.136	3.723	8.513
H24 plusSpiral	22336	6.182	6.232	3.345	8.593
H24 plusSpiral	22940	6.208	6.123	3.652	8.574
H24 plusSpiral	23311	6.206	6.144	3.682	8.557
H24 plusSpiral	26834	6.183	6.108	3.657	8.453